



TECHNISCHE
UNIVERSITÄT
WIEN

Vienna University of Technology

DIPLOMARBEIT

A Specimen Specific Finite Element Validation Study of Distal Radius Fracture Osteosynthesis

ausgeführt zum Zwecke der Erlangung des akademischen Grades eines Diplom-Ingenieurs
unter der Leitung von:

Assoc. Prof. Dr. Dieter H. Pahr
E317

Institut für Leichtbau und Struktur-Biomechanik

eingereicht an der Technischen Universität Wien
Fakultät für Maschinenwesen und Betriebswissenschaften

von

Alexander Synek
1128857
Schönbrunnerschlossstraße 31A/21
1120 Wien

Datum

Unterschrift

Abstract

Background: Volar plate osteosynthesis in distal radius fractures (DRF) is inherent to various complications. Finite element (FE) analysis could help to improve and compare current treatment approaches. Existing FE models do, however, lack adequate experimental validation. The goal of this study was to generate and validate specimen specific FE models of distal radius fracture (DRF) osteosynthesis in a semi-automatic fashion. The influence of local bone density and orientation on the validation results was conducted as a side study.

Materials and Methods: Biomechanical in-vitro experiments and specimen specific FE analysis were conducted on 34 fresh frozen, cadaveric human specimen with artificially created extra articular DRFs and volar locking plate osteosynthesis. The experimental spring stiffness was measured in uniaxial compression tests and compared to the elastic response of the FE models. QCT scans of the prepared samples were used to create the finite element models in rigorous accordance to the experiments. Local bone material data was incorporated based on HR-pQCT scans of the intact specimen. Three types of models were generated, with (a) density and fabric based bone material, (b) density based bone material and (c) homogeneous bone material. The finite element model stiffness was corrected for the machine compliance and linear regression analysis was performed to quantify the goodness of the predictions.

Results: All three types of FE models over-estimated the experimental stiffness but were significantly correlated to the experimental results ($p < 0.0001$). The coefficient of determination was similar for types (a) and (b) ($R^2 = 0.79$) but considerably lower for type (c) ($R^2 = 0.55$). Section forces at the screw-plate interface of the implant were evaluated in the FE models of type (a) and showed good agreement with experimental observations of screw-plate interface failures.

Conclusion: The elastic response of FE models with density based bone material was highly correlated with the experimental spring stiffness. The proposed semi-automatic model generation methodology paves the way for future parameter variation studies which enables the comparison of multiple treatment options.

Zusammenfassung

Hintergrund: Im Rahmen der Versorgung distaler Radiusfrakturen (DRF) mit volarer Platten-Osteosynthese kommt es immer wieder zu Komplikationen. Finite Elemente (FE) Analysen könnten helfen, existierende Behandlungsmethoden zu vergleichen und zu verbessern. Existierende FE Modelle sind allerdings unzureichend validiert. Ziel dieser Arbeit war es, Prüfstück-spezifische FE Modelle einer DRF-Osteosynthese mit Hilfe einer semi-automatischen Methodologie zu generieren und zu validieren. Der Einfluss der lokalen Knochendichte und -orientierung wurden im Rahmen einer Nebenstudie untersucht.

Material und Methoden: Biomechanische in-vitro Experimente und Prüfstück-spezifische FE Analysen wurden an 34 frisch eingefrorenen menschlichen Leichenknochen mit künstlichen, extra-artikulären DRFs und volarer Platten-Osteosynthese durchgeführt. Die experimentelle Federsteifigkeit wurde in einachsigen Kompressionsversuchen bestimmt und mit der Federsteifigkeit der FE Modelle verglichen. Die FE Modelle aller Prüfstücke wurden hierbei mit Hilfe von QCT Scans der präparierten Knochen erstellt. HR-pQCT Scans der intakten Knochen erlaubten die Einbindung lokaler Materialeigenschaften. Drei Typen von FE Modellen wurden generiert, wobei (a) dichte- und fabric-abhängiges Knochenmaterial, (b) dichte-abhängiges und (c) homogenes Knochenmaterial verwendet wurde. Die Federsteifigkeit der FE Modelle wurde von der Nachgiebigkeit der Prüfmaschine bereinigt und lineare Regressionsanalysen wurden durchgeführt um die Güte der Vorhersagen zu bestimmen.

Ergebnisse: Alle drei Typen von FE Modellen überschätzten die experimentelle Federsteifigkeit aber waren signifikant korreliert ($p < 0.0001$). Das Bestimmtheitsmaß der Modelltypen (a) und (b) war in etwa gleich ($R^2 = 0.79$), jedoch deutlich geringer bei Modelltyp (c) ($R^2 = 0.55$). Die Schnittgrößen am Schrauben-Platten-Interface des Implantats wurden in allen Modellen des Typs (a) ausgewertet und zeigten eine gute Übereinstimmung mit dem experimentellem Versagen des Schrauben-Platten-Interfaces.

Schlussfolgerungen: Die Federsteifigkeit von FE Modellen mit dichte-abhängigem Knochenmaterial war mit den experimentellen Ergebnissen hoch korreliert. Die präsentierte Methodologie zur semi-automatischen Modellerstellung ebnet den Weg für zukünftige Parameter-Variations-Studien und damit für den Vergleich verschiedener Behandlungsmethoden.

Acknowledgements

I would like to express my gratitude to all the people who supported me throughout the course of this thesis. This work would not have been possible without the help and guidance of my supervisor Dr. Dieter Pahr. I would also like to thank Dr. Sebastian Baumbach, an experienced surgeon, who did not only lend his brilliant mind but also his precious workforce to make the biomechanical experiments happen.

I express my thanks to the employees of the biomechanical laboratory of the Klinikum Grosshadern, in particular Dr. Yan Chevalier and Christian Schröder, for their support during the experimental part of this thesis. Similarly, I would like to thank Dr. Andreas Reisinger and Dr. Florian Toth for many fruitful discussions at the Institute of Lightweight Design and Structural Biomechanics.

Finally, I want to thank my friends and family for their moral support and patience throughout my whole education.

Contents

1	Introduction	1
1.1	Motivation	1
1.2	Distal Radius Fractures	1
1.2.1	Anatomy	2
1.2.2	Classification	3
1.2.3	Treatments	4
1.3	Research on DRF Treatment Methods	4
1.3.1	Clinical Studies	5
1.3.2	Experimental Studies	5
1.3.3	Computational Studies	6
1.4	Thesis Goals	8
2	Material and Methods	9
2.1	Biomechanical Experiments	10
2.1.1	Specimen Preparation	11
2.1.2	Mechanical Testing	13
2.1.3	Data processing	14
2.2	Finite Element Analysis	16
2.2.1	QCT Image Processing	20
2.2.2	HR-pQCT Image Processing	21
2.2.3	QCT to HR-pQCT Registration	23
2.2.4	Blender Modelling	24
2.2.5	Combining Image and Geometries	27
2.2.6	FE Model Assembly	29
2.2.7	FE model Solving and Postprocessing	36
2.3	Validation	37
2.3.1	Machine Compliance	37
2.3.2	Statistics	37
3	Results	39
3.1	Biomechanical Experiments	39
3.1.1	Experimental Stiffness and Yield Force	39
3.1.2	Correlation of Experimental Stiffness and Yield Force	40
3.1.3	Failure Mechanism	42
3.2	Finite Element Analysis	42
3.2.1	Stiffness	42

3.2.2	Deformation	43
3.2.3	Stresses	44
3.2.4	Damage	45
3.2.5	Screw-Plate Interface Forces	46
3.3	Validation	47
3.3.1	Full Model Valdiation	48
3.3.2	Influence of the Machine Compliance	50
3.3.3	Influence of the Bone Material Model	51
3.3.4	Influence of the Screw Types	52
4	Discussion	54
4.1	Biomechanical Experiments	54
4.2	FE Analysis	55
4.3	Validation	56
4.4	Limitations	57
4.5	Conclusion	57

List of Figures

1.1	Rough overview of the anatomy of the human forearm and wrist	2
1.2	Detailed anatomy of the distal radius	2
1.3	AO-classification of DRFs	3
1.4	DRF open reduction and internal fixation with a volar plate	4
1.5	Biomechanical experiments on DRF treatments	5
1.6	Typical approach of generating FE models of DRF treatments	7
2.1	Design of the validation study	9
2.2	Outline of the biomechanical experiments	10
2.3	Osteosynthesis material and hole numbering of the implant	11
2.4	Simulation of the extraarticular fracture	12
2.5	Specimen alignment with the custom made jig	12
2.6	Process of specimen embedding	13
2.7	Test setup and loading protocol of the biomechanical experiment	14
2.8	Cropping and shifting of the dataset	15
2.9	Computation of the elastic range and the spring stiffness	16
2.10	Schematic comparison of experimental setup and FE model	17
2.11	Data flow in the FE model generation	19
2.12	Exemplary QCT image histogram and 3D representation	20
2.13	QCT image segmentation and surface generation	21
2.14	HR-pQCT image processing and bone surface generation	22
2.15	Semi-automatic registration of the QCT and HR-pQCT derived bone surfaces	23
2.16	Overview of the four components of the Blender template file	25
2.17	Implant template modelled in Blender	25
2.18	Fracture gap and proximal embedding as modelled in Blender	26
2.19	Distal embedding modelled in Blender	26
2.20	Alignment of the Blender geometries to the QCT derived surfaces	27
2.21	Generation of the combined image	28
2.22	Generated mesh and improvement by spike elimination	29
2.23	Bone material mapping for an exemplary specimen	31
2.24	An exemplary FE model with boundary conditions	35
2.25	Screw-Plate interface connector and local orientation	36
3.1	Cumulative plot of the 34 load-displacement curves	40
3.2	Linear regression of the experimental stiffness and yield force	41
3.3	Exemplary screw-plate interface failure and histogram	42
3.4	Deformation plots of three samples in volar and lateral view	43

3.5	Bone and implant stress plots of three samples	44
3.6	Exemplary plots of the damage variable	45
3.7	Orientations of force and moment vectors at the screw-plate interface of a single specimen	46
3.8	Averaged section forces and moments at the screw-plate interface. Scales for the forces and moments are provided in boxes (A) and (B), respectively.	47
3.9	Linear regression of the full FE model	48
3.10	Bland Altman plot of FEA and experimental stiffness	49
3.11	Validaton with and without correction for machine compliance (MC)	50
3.12	Validaton with simple and complex bone material models	51
3.13	Validaton with separated screw types	53

List of Tables

2.1	Overview of the material modelling approach	17
2.2	Modelling of the material interfaces	17
2.3	Elastic material constants of bone	32
2.4	Yield material constants of bone	33
3.1	Results of the biomechanical experiments	39
3.2	Results of the linear regression of the experimental stiffness and yield force	41
3.3	Results of the FE analysis	42
3.4	Results of the linear regression with the full FE model	49
3.5	Influence of the machine compliance (MC) on the linear regression	50
3.6	Overview of the bone material symmetries and homogeneity	51
3.7	Influence of the bone material model on the linear regression	52
3.8	Influence of the screw type on the linear regression	52

Chapter 1

Introduction

1.1 Motivation

Distal radius fractures (DRF) are among the most common fractures of the human skeleton and predominantly affect the elderly. With increasing life expectancy, augmented incidence and demands on DRF treatments are anticipated in the future. Thus, the development of cost and time efficient procedures with minimal complications is essential.

The performance of novel DRF treatment methods is currently subject of numerous clinical, experimental and computational studies. In general, computer simulations represent a cheap and fast alternative to experimental studies. Simulations allow multiple virtual tests on a single specimen, thereby, eliminate inter-specimen variability and enable extensive parameter variation studies. However, existing simulations lack adequate experimental validation. The interpretation of the results and the transfer to clinical practice is therefore limited.

The goal of this thesis was to generate and experimentally validate specimen specific FE models which allow to predict the biomechanical performance of DRF treatments. Maximum variability and minimal manual intervention of the modelling procedure were aspired to facilitate comparisons of treatment variations in the validated model.

1.2 Distal Radius Fractures

DRFs are common fractures of the radial bone which are located close to the wrist [1]. Due to the proximity to the wrist, DRFs might impair the joint functionality [2]. Basic knowledge about wrist and forearm anatomy is therefore crucial for understanding the emergence and implications of DRFs and will be introduced briefly in the following. The presented anatomical content is based on Marieb et al. [3] if not denoted differently. Additionally, an overview of current treatment strategies is included in order to outline the diversity of existing approaches.

1.2.1 Anatomy

Radius and ulna form the skeleton of the forearm (see Figure 1.1) and belong to the group of long bones. As such, they consist of a shell of dense, cortical bone filled with spongy, trabecular bone. Cortical regions are most pronounced in the shaft while trabecular bone constitutes the main part of the ends of the radius [4]. On the proximal end, radius and ulna articulate with the humerus and form the elbow joint. Distally, the wrist joint is formed with the carpal bones. Radius and ulna are connected by the interosseous membrane and articulate at two regions, namely the proximal and distal radioulnar joint.

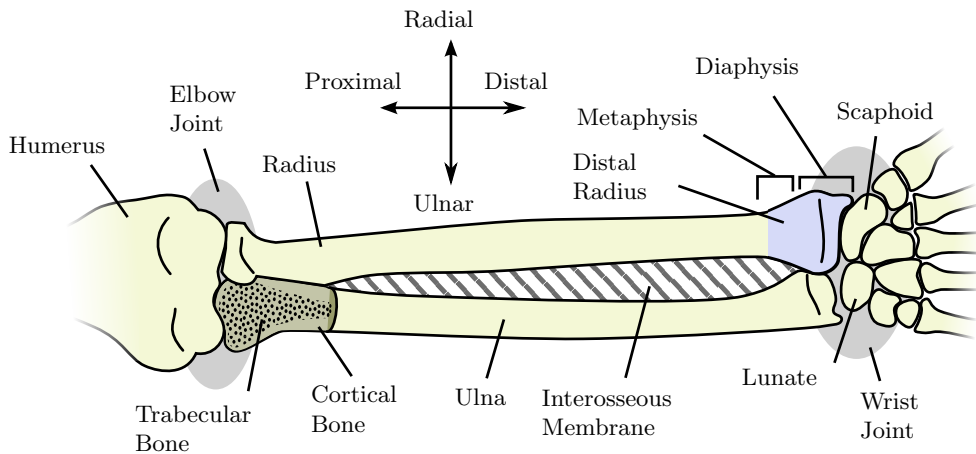


Figure 1.1: Rough overview of the anatomy of the human forearm and wrist

The distal radius is the region of the radial bone which is close to the wrist (see Figure 1.2). It is anatomically characterized by the radial styloid process, the ulnar notch and a concave groove in between. The groove is further separated into the fossa scaphoidea and lunata [5, 6] and majorly contributes to the functionality of the wrist joint by articulating with the scaphoid and lunate carpal bone, respectively.

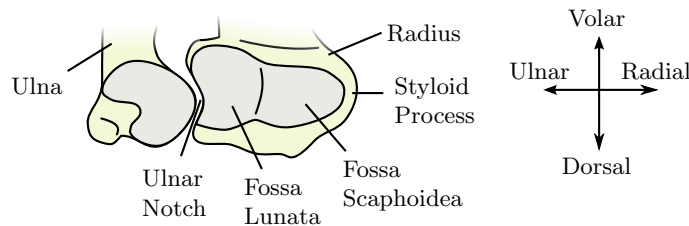


Figure 1.2: Detailed anatomy of the distal radius

The ellipsoidal joint formed by the radius and the carpals is called the radiocarpal joint and allows wrist flexion and extension as well as radial and ulnar flexion [7]. Injuries at the wrist most often result from falling on the outstretched hand [1], which forces the wrist in extreme extension. A frequent consequence is the fracture of the distal radius, as the metaphyseal region is low in density [5] and absorbs most of the energy of a fall [7].

1.2.2 Classification

A widely used classification of long bone fractures is provided by the AO-foundation [8] and was originally proposed by Müller et al. [9]. Both location and fracture morphology are assigned a unique sequence of numbers and letters to ensure not only proper documentation but also to provide quick support for prognoses and treatment decisions. The AO-classification of DRFs is outlined in Figure 1.3.

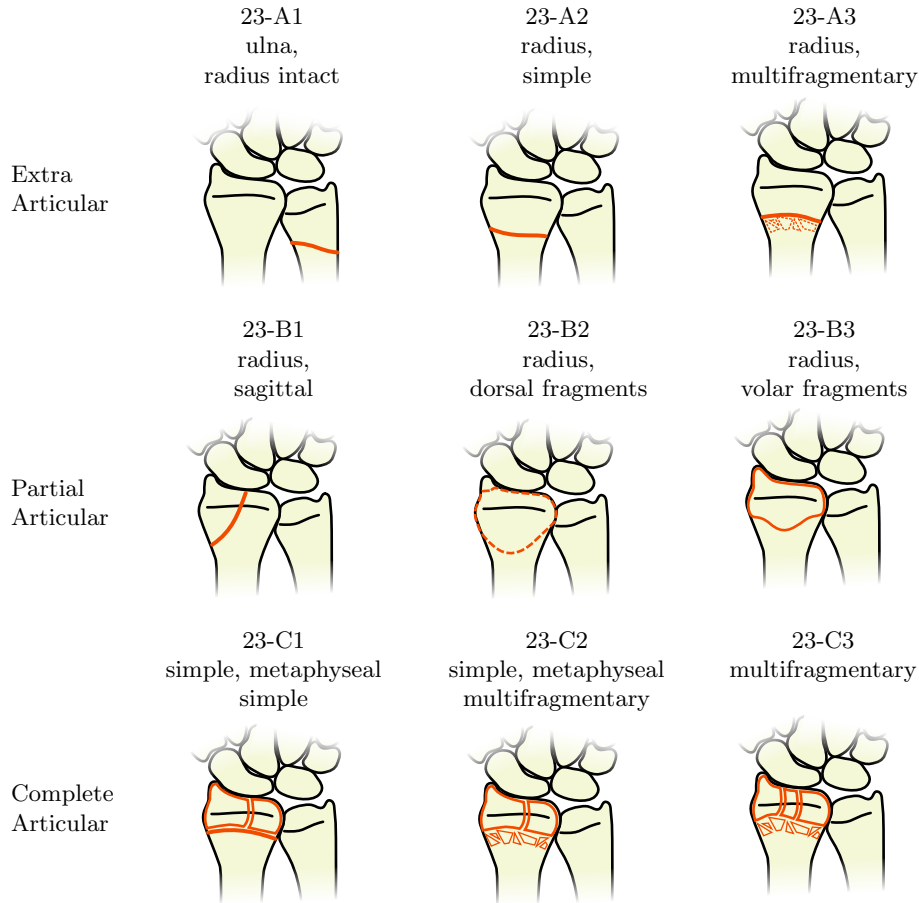


Figure 1.3: AO-classification of DRFs

The location of the distal radius is identified by the numbers '2' for radial and ulnar bone and '3' for the distal segment. Fracture morphology is indicated by letters 'A' to 'C' and categorized into the following groups: Extraarticular, partial articular and complete articular. Extraarticular fractures do not extend to the articular surface, whereas partial and complete articular fractures involve partial or complete separation of articular components of the bone. An additional number refines the fracture morphology by including the complexity of the fracture. For instance, a 23-C3 fracture represents a complete articular DRF with both complex articular and metaphyseal fracture morphology.

1.2.3 Treatments

Depending on the severity of the fracture, DRFs can lead to long term functional impairment, pain and deformity [2, 10]. Common complications include osteoarthritis, limited range of motion, malunion of the bone and radial shortening.

The AO-foundation offers recommendations for the treatment of each DRF type which should minimize complications and ensure good clinical outcomes [11]. Restoring and maintaining the correct anatomy of the distal radius is the goal of any treatment method. The process of restoring the anatomy is called reduction and can be performed either closed or open, i.e. with or without surgical intervention. Maintenance of the reduction of the DRF is ensured by the use of plaster cast, wrist bridging or nonbridging external fixation, pins, volar or dorsal plates, bone scaffolds or bone cement [5, 11, 12]. The whole procedure of fracture reduction and fixation with an implantable device is referred to as osteosynthesis. An exemplary treatment of a DRF with open reduction and volar plate fixation is displayed in Figure 1.4.

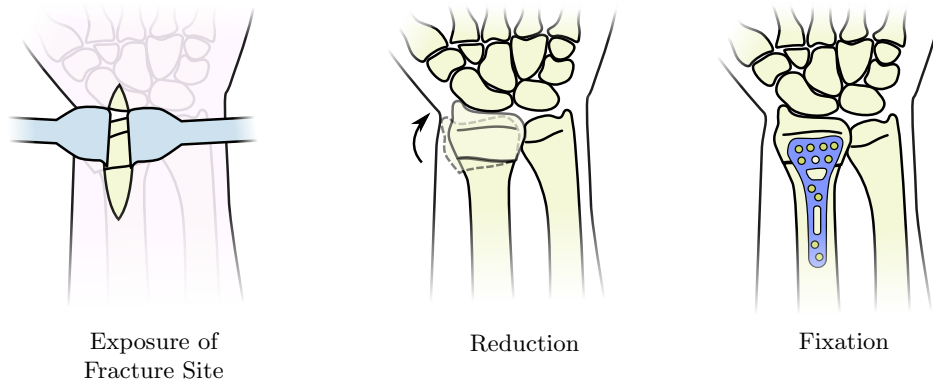


Figure 1.4: DRF open reduction and internal fixation with a volar plate

DRF treatment options are not limited to the type of reduction and osteosynthesis device. Additional decisions have to be made on device specific parameters. For instance, internal fixation with volar plates can be performed with varying numbers [13, 14] of locking or nonlocking [15], fixed or variable angle screws [16, 17]. Locking screws have screwheads with threads which cut into the plate and constitute a rigid plate-screw construct. The angle of the screw with respect to the implant plate is either fixed, i.e. predefined by the manufacturer, or variable.

1.3 Research on DRF Treatment Methods

Although there is a trend towards open reduction and internal fixation with volar plates [18, 19], the optimal therapeutic approach remains a topic of research [20]. Numerous clinical, experimental, and computational studies have been conducted to compare existing and investigate novel treatment strategies. Not only fracture treatments but also research methods have evolved and are presented in the following.

1.3.1 Clinical Studies

The safety and efficiency of medical treatments is studied by clinical trials. They provide the strongest evidence in medical research and often influence clinical practice [21].

Outcome parameters of clinical studies are generally limited to in-vivo measurements [22, 23, 24, 25]: A goniometer and a hand dynamometer allow to determine the wrist range of motion and grip strength, respectively. Fracture fragment displacements, i.e. loss of reduction, can be detected in radiographs. Additionally, patient subjective parameters such as the perceived pain can be quantified. All those parameters are evaluated in multiple follow-up examinations after the treatment and monitored over periods ranging from months to several years. Subsequently, treatment methods can be compared quantitatively based on the achieved scores.

It is evident that clinical studies essentially contribute to the development of novel DRF treatments but also have inherent drawbacks. Disadvantages include the extensive time frame, high cost, participant recruitment and ethical issues [21]. Also, the participant heterogeneity might influence the study results even if treatments are assigned randomly to the patients. This holds in particular for studies with small groups.

1.3.2 Experimental Studies

Experimental studies are conducted in-vitro and always simplify the physiological situation (see Figure 1.5). Compared to clinical studies, the testing conditions of in-vitro experiments can be defined more precisely and allow observing additional variables which are not accessible in-vivo.

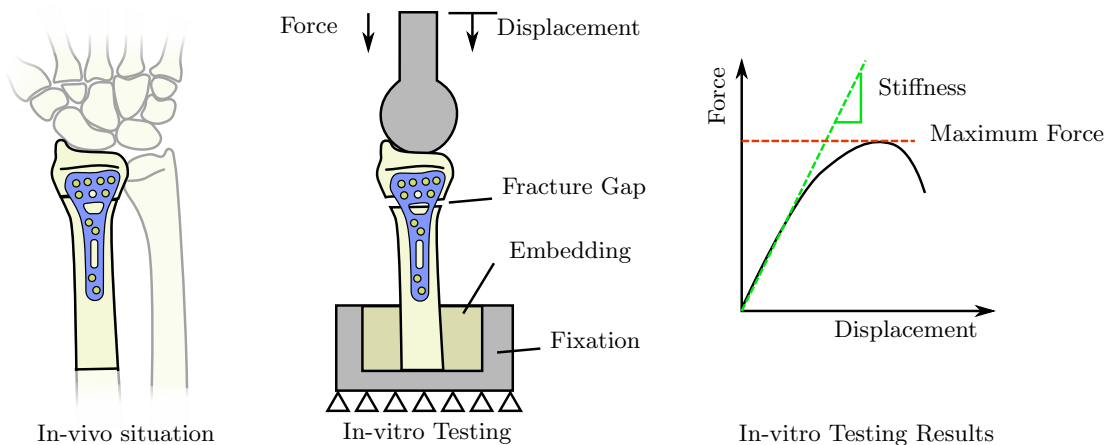


Figure 1.5: Biomechanical experiments on DRF treatments

Experimental studies on DRFs have been performed on cadaveric forarms [26, 27, 28] or isolated radii [29, 30, 31] of humans but also on synthetic bone [13, 32, 16]. The treatment procedure is typically simulated by creating an artificial fracture, followed by fracture fixation with an osteosynthesis device. Load is applied to the samples in a material testing machine

to mimic physiological loading at the wrist. The loading protocols vary from monotonic [16] to cyclic [29] in order to determine the mechanical performance immediately after the surgery or during the rehabilitation phase. Commonly, force and displacement are recorded during uniaxial compression tests and used to compute the apparent stiffness and maximum force of the bone-implant system [32, 16]. Other authors evaluated the residual displacement of the fracture fragments after testing [13, 33]. Cyclic loading allows to measure additional parameters such as the number of cycles to failure and loss of reduction [31].

Obvious limitations of experimental studies are the lack of muscle and stabilizing soft tissue around the bone [13, 34, 33], the possibly unphysiological loading conditions [19, 35, 36] and the absence of bone healing particularly in cyclic testing [34]. Experiments on cadaver bone also entail the disadvantages of large inter-specimen variability and limited specimen availability. Despite these limitations, experimental studies on DRFs have proven to deliver results which are relevant for clinical practice [37].

1.3.3 Computational Studies

Computational studies involve the simulation of biomechanical experiments based on mathematical models and their numerical solution. A widely used numerical method to predict the mechanical behavior of solids and structures is the FE method [38]. It became a standard tool in classical engineering and has also gained popularity in the field of biomechanics [39].

The general principle of the FE method is to approximate the solution of an equation over a large domain by splitting it up in small, non-overlapping subdomains, i.e. finite elements, which can be formulated and solved in a discrete way [40]. In solid mechanics, three-dimensional (3D) bodies are discretized by numerous continuum elements such as hexahedra or tetrahedra which are defined by a set of nodes. The deformation of each element is determined by a function which relates nodal forces to nodal displacements based on the given material properties. External loads and constraints can be imposed on any node and constitute the boundary conditions. Given all elements and nodes, material properties and the boundary conditions, a global system of equations can be established and solved for unknown forces and displacements to satisfy static or dynamic equilibrium conditions [41].

An evident prerequisite for simulating biomechanical experiments with the FE method is an accurate representation of the bone morphology, i.e. geometry and architecture, and material behavior. Computed tomography (CT) has proven to be useful for providing both morphometric and material parameters and, therefore, often serves as a basis for FE analysis [42]. CT is a 3D imaging technique which is based on X-rays [43]. In CT devices, multiple two-dimensional (2D) radiographs are recorded around a single axis of rotation and used to reconstruct a 3D image. The 3D image is a spatial representation of the bone which consists of small cuboids, called voxels, which are assigned grey values depending on its cumulative absorption of X-rays. Quantitative CT (QCT) scans are calibrated such that the amount of absorption relates to the bone mineral density (BMD) [44] which is an indicator for the bone's mechanical competence [45]. Thus, both information on the material and the morphology of the bone are captured in the CT images. Clinical QCT scans can be performed on peripheral and central sites [44] and typically result in images with voxel sizes in the millimeter range [43]. High resolution peripheral QCT (HR-pQCT) devices are capable of generating images with

voxel sizes of approximately 0.1 mm in vivo but their application is restricted to peripheral regions [46]. FE models of bone can be created either by direct conversion of each voxel to a hexahedral finite element or by creating smooth meshes based on a reconstructed bone geometry [47]. In case the image resolution is too low to capture the trabecular structure, the whole bone is modelled as a continuum and homogenized material properties are assigned to the elements as a function of the corresponding grey values from the CT scan [41]. Previously, smooth homogenized FE models of the intact radius have been presented which were in good agreement with experimental results [48].

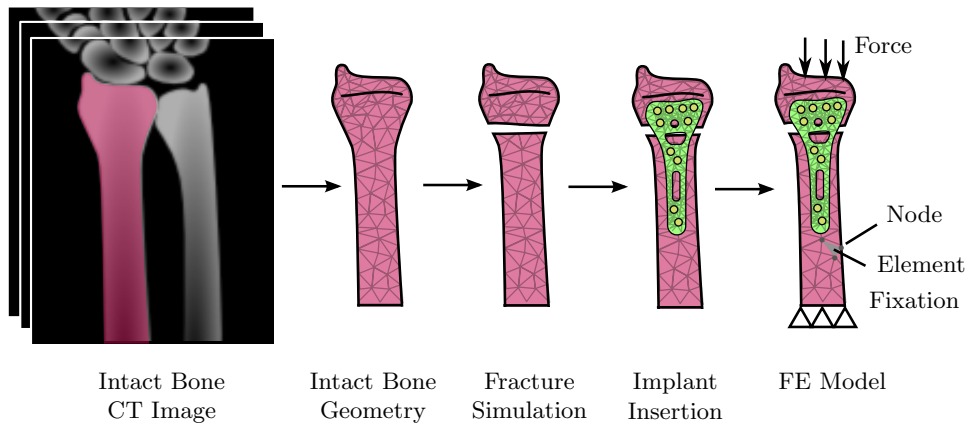


Figure 1.6: Typical approach of generating FE models of DRF treatments

FE simulations of fracture treatments involve not only bone, but also the implant system. A common approach to modelling the bone-implant system is to reconstruct the bone geometry from CT data, to virtually remove material to simulate the fracture and to insert the 3D geometry of the implant [49, 50, 51, 52] (see Figure 1.6). Several material interfaces need to be accounted for in the simulation: Bone-screw, screw-plate, and bone-plate. Bone-screw and screw-plate interfaces are typically assumed to be fully bonded whereas contact is defined between bone and implant plate. Compared to FE models of intact bone, fracture treatment simulations involve less sophisticated material models of bone. Cortical and trabecular regions were separated in the studies of Lin et al. [49] and Cheng et al. [51] but simply assigned homogeneous, isotropic material properties. Boundary conditions and loads were imposed on these models in accordance with biomechanical experiments. Commonly, movements of the bone shaft are constrained and forces are applied on a set of nodes at the distal end of the radius. The averaged displacement of the nodes of the fracture fragment is then used to compute the spring stiffness of the bone-implant system.

None of the FE simulations of DRF treatments which are known by the author was validated adequately with experimental data. Lin et al. [49] and Cheng et al. [51] compared the predicted spring stiffness to published experimental data. The quality of this validation approach is questionable as experimental test setups and results vary considerably [37]. Mair et al. [52] conducted both experiments and simulations but limited the validation procedure to comparing the FE results of a single specimen to the averaged experimental data of multiple specimen.

1.4 Thesis Goals

It could be shown that clinical trials as well as experimental and computational studies are essential to developing novel DRF treatments. FE simulations have great potential to eliminate drawbacks of biomechanical experiments and to provide a deeper insight into the mechanisms of the bone-implant system. Multiple treatment methods could be applied and evaluated in a single specimen to exclude inter-specimen variability and even extensive parameter variation studies could be conducted. Internal variables such as element stresses could reveal the weakest links and provide a basis for improvements of the implant system.

There are, however, three major limitations of DRF treatment FE models in literature:

- (i) *The models were validated inadequately:* Non-validated FE simulations might be useful for preliminary intra-study comparisons of treatment strategies but their clinical relevance is severely impaired
- (ii) *The model generation procedures required considerable manual intervention:* Manual intervention in the model generation procedure impedes large scale parameter variation studies
- (iii) *Highly simplified bone material models were used:* Bone density and orientation might have a pronounced influence on the mechanical properties of the FE model

Accordingly, the primary goals of this thesis were defined as follows:

- (1) Experimental validation of the FE model spring stiffness on a reasonable sample size
- (2) Development of a semi-automatic, specimen specific FE model generation procedure

With a secondary objective:

- (3) Investigation of the influence of local bone density and orientation on the FE model

In particular, the model generation and validation will be performed on a large sample ($n > 30$) of human cadaveric radii with artificially created fractures and volar locking plate osteosynthesis.

Chapter 2

Material and Methods

This validation study was based on biomechanical experiments and specimen specific FE models of 34 cadaveric human radii with artificially created fractures and volar locking plate fixation. The study design is outlined in Figure 2.1.

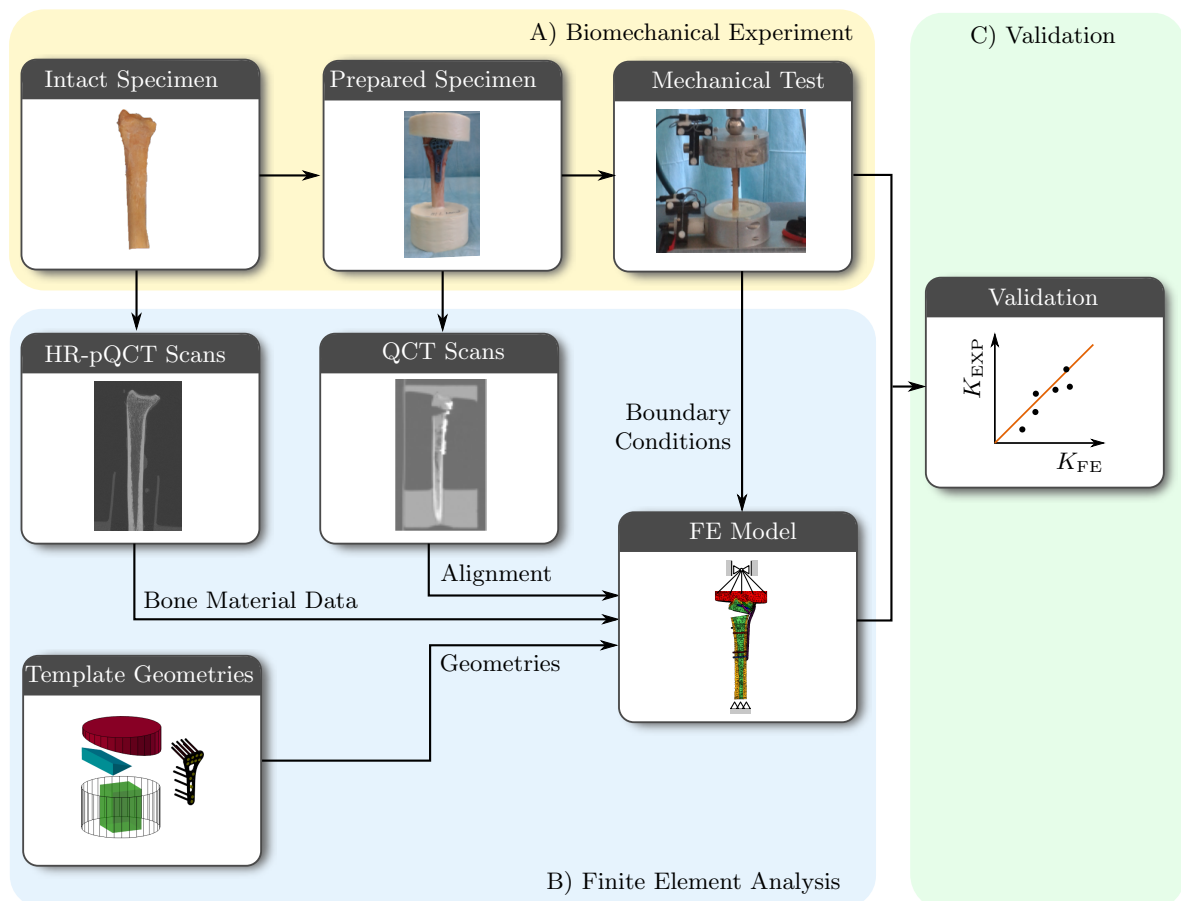


Figure 2.1: Design of the validation study

Biomechanical tests were performed on all cadaveric radii in order to determine the experimental spring stiffness K_{EXP} of the bone-implant system (see Figure 2.1 A). HR-pQCT scans of the intact and QCT scans of the prepared radii were done prior to testing. Template geometries of the embedding, fracture gap and implant were generated and used in conjunction with the scans to reproduce the biomechanical tests in an FE analysis. This approach allowed to include specimen specific bone material data from the HR-pQCT scans and alignment of the embedding, fracture gap and implant geometries as indicated in the QCT scans (B). The spring stiffness of the FE model K_{FE} was then computed and compared to the experimental results in order to assess the predictive capabilities of the models (C).

The following sections are structured in accordance to Figure 2.1 and present the biomechanical experiments (A), the FE analysis (B) and the validation procedure (C) in detail.

2.1 Biomechanical Experiments

The presented biomechanical experiments were originally conducted to compare different screw lengths and screw types in volar plate osteosynthesis of DRFs in human cadaveric bone. Both studies were approved by the ethics committee of the Ludwig Maximilians University Munich (LMU #409-13). The content of this section is limited to the general procedure of preparing and testing the specimen as well as the data processing required to compute the apparent stiffness. An overview of all necessary steps is displayed in Figure 2.2.

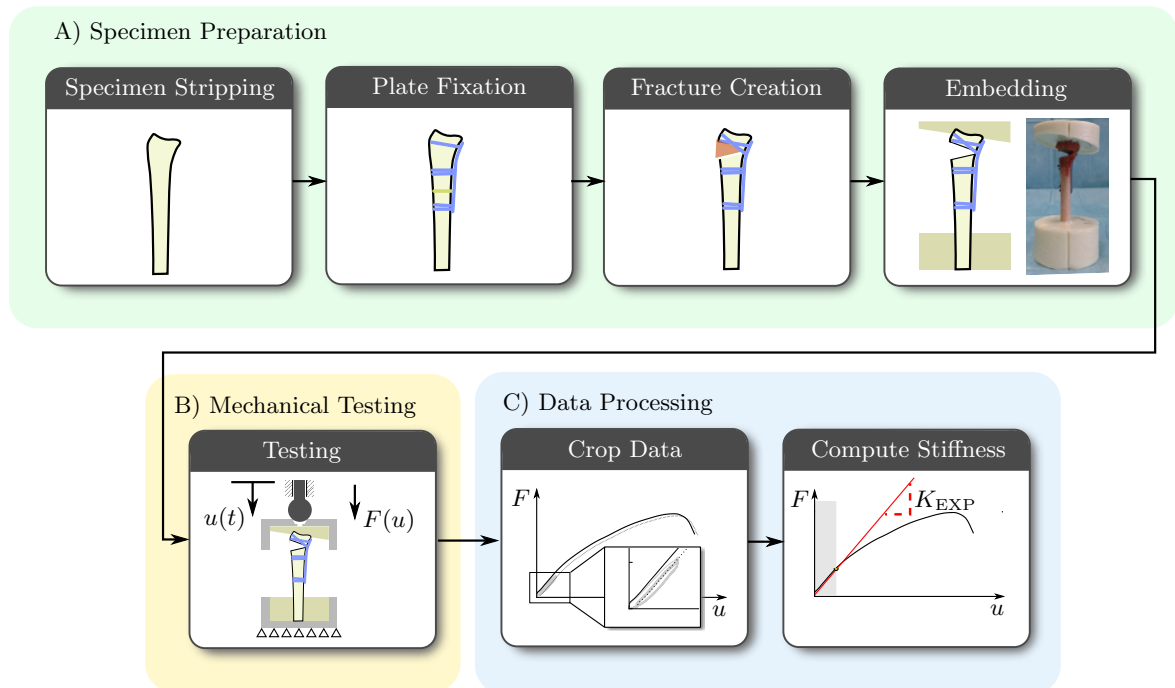


Figure 2.2: Outline of the biomechanical experiments

The specimens were stripped from soft tissue and prepared by mounting a volar locking plate, creation of a fracture gap and adding a proximal and distal embedding (see Figure 2.2 A). Uniaxial compression tests were performed on the prepared specimens in a material testing machine (B). Recorded force and displacement data was then cropped to the relevant range and used to automatically compute the spring stiffness K_{EXP} of the bone-implant system. The following sections explain steps A to C in more detail.

2.1.1 Specimen Preparation

34 fresh frozen radii were obtained from the Centre of Anatomy and Cell Biology, Medical University of Vienna, Austria and stored in a freezer at -18°C . Specimens were thawed prior to preparation but not longer than 24 hours before conducting the mechanical tests. Plate fixation and fracture gap creation were performed by an experienced surgeon.

All specimen were cut to a uniform length of 140 mm and the soft tissue was removed. Variable angle volar locking plates (Aptus 2.5 Adaptive TriLock Distal Radius Plates, Volar, A-4750.61/.62, Medartis Inc., Basel, Switzerland) with a thickness of 2mm were then mounted to the bone as follows (see Figure 2.3): First, the plate was positioned on the radius such that the distal contour of the plate was just proximal to the volar rim of the distal radius. The plate was fixed in this position by drilling a pilot hole with a 2mm drill and inserting a 2.5mm nonlocking screw (Medartis A-5700) in the implant hole number 11. Additionally, 2.5mm locking screws (Medartis A-5750) were inserted into holes number 9, 10, 12 and 13. A drill guide block (Medartis A-2723.01/.02) was then used to drill pilot holes and to insert screws in the most distal row, i.e. screws number 1 to 4. The nonlocking screw in hole number 11 was then removed again.

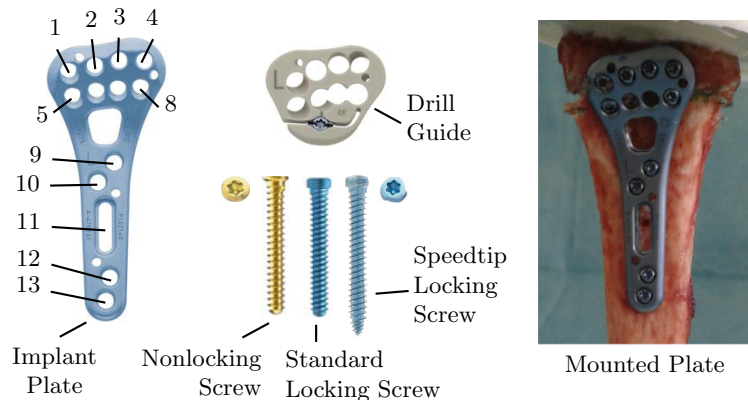


Figure 2.3: Osteosynthesis material and hole numbering of the implant

A wedge with an opening of 10mm was cut out of the bone with an oscillating handsaw to simulate a simple extraarticular fracture (AO 23-A3) as shown in Figure 2.4. The wedge was located dorsally 8mm and volarly 10mm proximal to the dorsal and volar rim of the distal radius, respectively. This fracture location was previously identified in CT scans of patients with DRFs by Baumbach et al. [53]. Both the volar and dorsal cortices were completely separated and the fracture fragments were neglected. Thus, this fracture model represents a worst-case scenario of an extraarticular DRF.

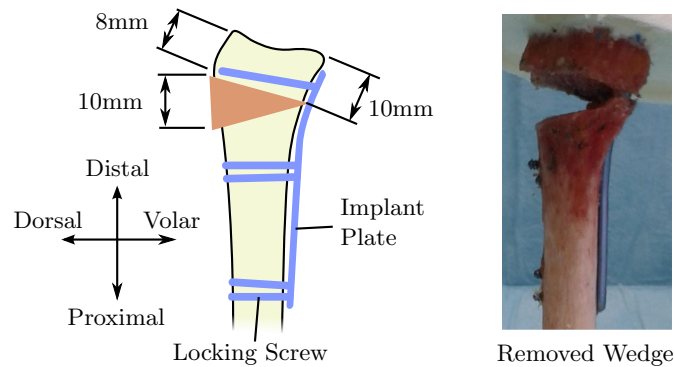


Figure 2.4: Simulation of the extraarticular fracture

After the wedge was removed, screws number 6 and 8 were pre-drilled and inserted with the drill guide block. Standard locking screws were used for all 10 screw positions in 26 out of 34 specimen. Self drilling prototype speedtip screws were used for the 6 distal screw positions in the remaining specimen which allowed to omit the step of pre-drilling. The lengths of the 6 distal screws were determined by measuring the distance from the implant plate to the dorsal cortex of the radius along the pilot hole using a depth gauge (Medartis A2730/.01): In 9 specimen with standard locking screw, the lengths were chosen as close as possible to the measured distance. Protrusion of the dorsal cortex was, however, avoided in any case. A target of 75% of the measured length was chosen for the distal screws of the remaining samples.

All specimens were embedded proximally and distally with polyurethane (SG141/PUR145, FDW Handelsgesellschaft, Austria). The whole embedding procedure was standardized with a custom made alignment jig [48, 54] to ensure uniform alignment with respect to the testing machine (see Figure 2.5).

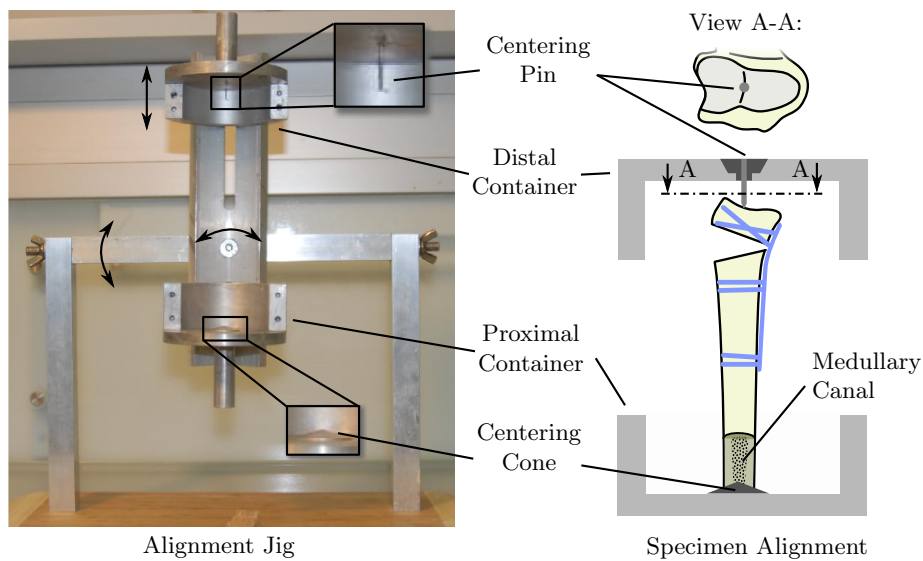


Figure 2.5: Specimen alignment with the custom made jig

The jig consisted of a proximal and a distal container which were mounted to a guide rail to adjust the container distance. Two axis of rotation were incorporated to create an inclined distal embedding. Both containers were demountable into two half cylinder shells. Rectangular alignment plates could be inserted in between the half cylinder shells to create a notch in the embedding. The bones were aligned proximally at the medullary canal and distally at the center of the ridge subdividing the scaphoid and lunate fossa with a centering cone and pin, respectively. Rotation around the shaft was standardized by aligning the volar plate co-planar with the alignment plates.

Following specimen alignment, the proximal container was arranged horizontally and embedding material was inserted to a height of 40 mm (see Figure 2.6). After curing of the proximal embedding, the distal embedding was created. To avoid air being trapped in the concavity of the articular surface, a temporary mold was created with plasticine and filled with a small amount of embedding material.

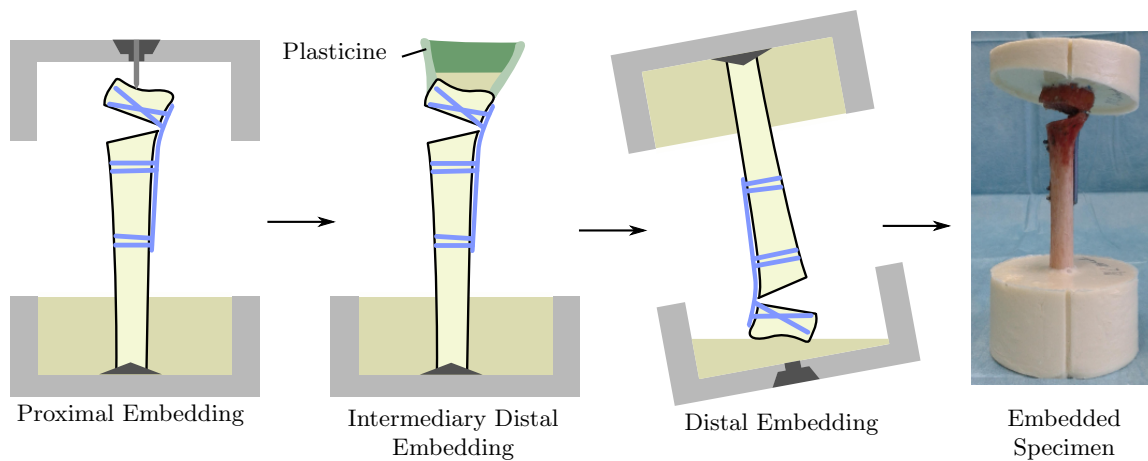


Figure 2.6: Process of specimen embedding

The plasticine was removed after curing and the radius was turned upside down and aligned such that the articular surface was approximately horizontal. The distal container was then filled with embedding material until the rim of the articular surface was covered shallowly. After a final curing period, the embedded specimens were removed from the proximal and distal container.

2.1.2 Mechanical Testing

Following preparation, the specimens were mounted in an electromechanical material testing machine (Z010/TN2A, Zwick GmbH & Co. KG, Ulm, Deutschland) to conduct uniaxial compression tests (see Figure 2.7). Proximally, the samples were fixed to an aluminium plate with the container originally used for the embedding procedure. The second container was clamped to the distal embedding.

A centering hole in the distal container was used in conjunction with a 32mm steel sphere to form a ball joint which allowed distal fragment rotation. Friction at this joint was minimized by applying lubricant. The whole assembly of specimen, proximal and distal container was manually aligned with the loading axis of the machine by centering the steel sphere to the centering hole. Bar clamps were used to ensure that the aluminium plate would not shift.

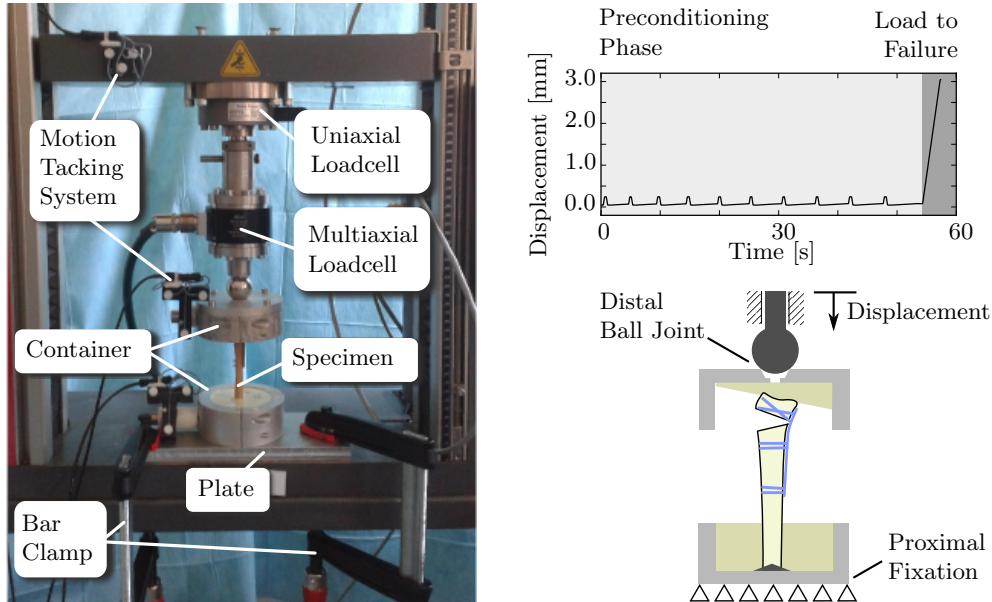


Figure 2.7: Test setup and loading protocol of the biomechanical experiment

A preload of 10N was applied prior to testing to ensure that the steel sphere is in contact with the container. After the preload was reached, 10 cycles of 0.2mm displacement were imposed at 1mm/s to exclude settling effects from the final loading cycle [48]. The specimens were then loaded at a displacement rate of 1mm/s until either 3mm displacement or a force drop of 20% was reached.

Force and displacement were recorded during the test by utilizing the output of the standard uniaxial load cell and linear encoder of the testing machine. Data of a multiaxial load cell and an ultrasound motion tracking system were additionally gathered but not used in this validation study.

2.1.3 Data processing

A custom Python script was developed in order to compute the spring stiffness of the bone-implant construct automatically. The spring stiffness is defined as a constant which linearly relates the measured force to the imposed displacement. This relationship holds until the elastic limit or yield point is reached and damage or permanent deformation is gradually induced.

Measured forces and displacements of the experiments served as the basis for computing the spring stiffness. An exemplary dataset is visualized as a force-displacement plot in Figure 2.8. This data needed to be cropped to exclude the preconditioning cycles.

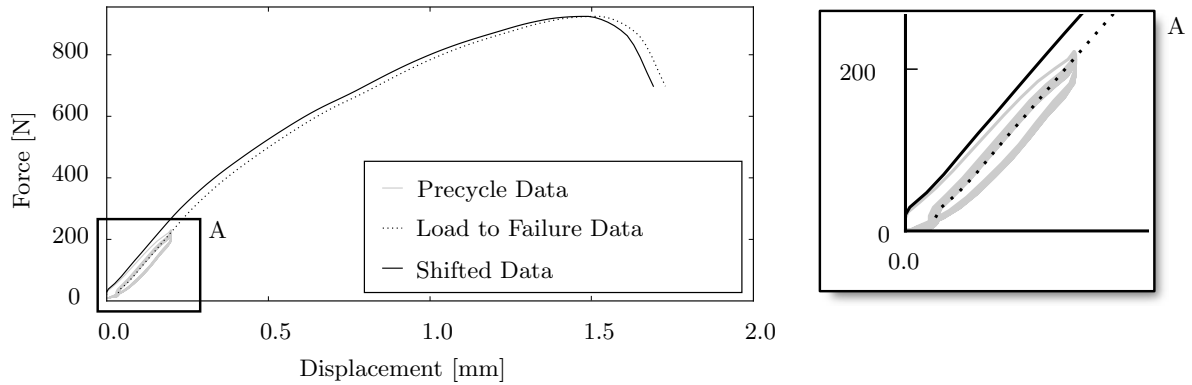


Figure 2.8: Cropping and shifting of the dataset

Data cropping was performed by a reverse search on the recorded force data. Starting from the last data entry, the first value below a given force limit was selected. A limit of 20N was chosen in order to compensate for an initial nonlinear region due to misalignments between the distal container and the steel sphere. The first pair of force-displacement values below and the first pair of values above 20N were then linearly interpolated to find the displacement at 20N. This displacement was subtracted from the measured values such that all curves started at a displacement of 0mm and a force of 20N.

The cropped and shifted dataset was then used to find the elastic range as shown in Figure 2.9. This range is characterized by a linear relationship between force and displacement which can be formulated as a straight line. Increasing deviations from this straight line indicate the end of the elastic range and the start of damage or plasticity. For an automatic determination of the elastic range, straight lines were fitted to an incrementally expanding data set. The best fit of the straight line would then imply the end of the elastic region and its slope would define the spring stiffness.

The straight lines were fitted to the data by using the linear regression function implemented in the Scientific Python (SciPy) library of Python. This function returns the slope and intercept of a straight line which minimizes the squared distances to the data points. The coefficient of determination R^2 was computed to quantify the goodness of the fit. It is defined as the ratio of the variance explained by the regression model to the total variance of the data [55]. The coefficient of determination approaches an optimal value of 1 in case the model is capable of fully covering the data set variance.

In practice, an initial range of 5 data points was chosen and the coefficient of determination was computed. Another data point was added and the linear regression was performed again. This process was repeated until the end of the data set was reached. The force and displacement at which R^2 reached its maximum was then picked as the limit of the elastic range. The slope of the regression system of this range was defined as the experimental spring stiffness of the bone-implant system.

Possible relations between the force at the elastic limit, i.e. the yield force, and the spring stiffness were then investigated in a linear regression analysis. This analysis was conducted in analogy to the final validation process which is described in Section 2.3.

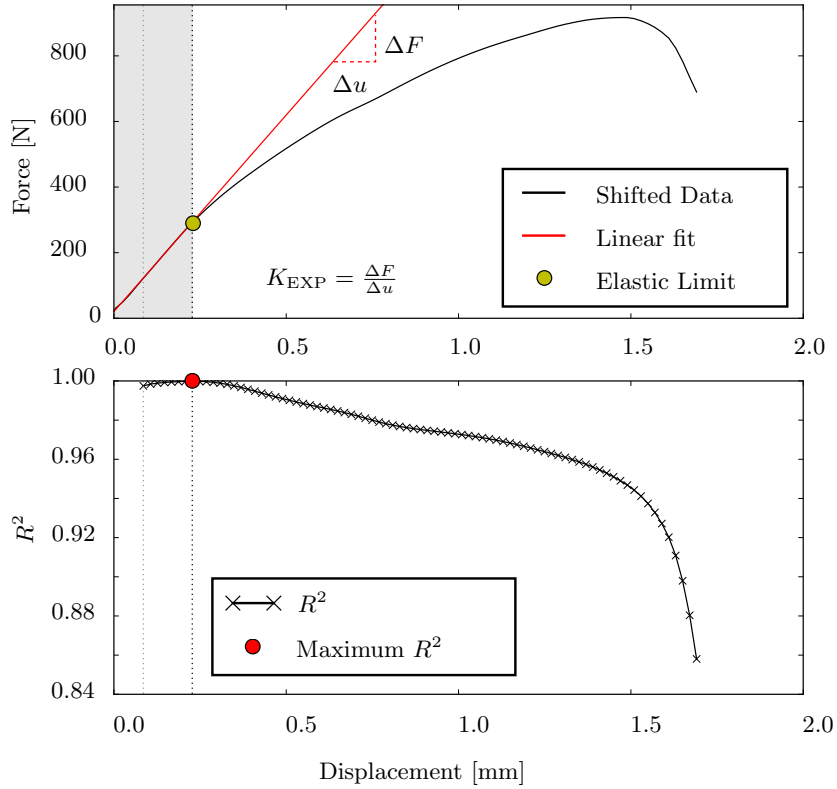


Figure 2.9: Computation of the elastic range and the spring stiffness

2.2 Finite Element Analysis

The goal of the finite element analysis was to reproduce the biomechanical experiments numerically. For this purpose it was necessary to generate FE models which are specifically adapted to the tested specimen. The FE model specification and generation will be outlined briefly in the following to provide an overview of subsequent sections.

The approach of modelling the geometry, materials and material interfaces is summarized in Figure 2.10, Table 2.1 and Table 2.2. Individual bone, implant, fracture gap and embedding geometries were included in the model. Implant screws were simplified as cylinders without threads and pre-drilled holes were neglected. A truncated cylinder with reduced diameter represented the distal embedding to decrease the model size. The proximal embedding was excluded from the model. Instead, the shaft of the bone was cut at its proximal plane.

The cortical and trabecular region of the bone were separated and modelled as visco-plastic, damagable and inhomogeneous materials. Cortical bone material was modelled as isotropic with density dependent material. Orthotropy was assumed for trabecular bone and material properties determined based on density and local bone architecture. Models with more simple bone material models were created as a side study and are described in Section 2.2.6. Implant, screws and embedding were modelled as linear elastic, isotropic and homogeneous materials. Interfaces between screws and bone as well as screws and implant plate were defined as fully bonded. Nodes of the implant plate and bone were separated but no contact was defined.

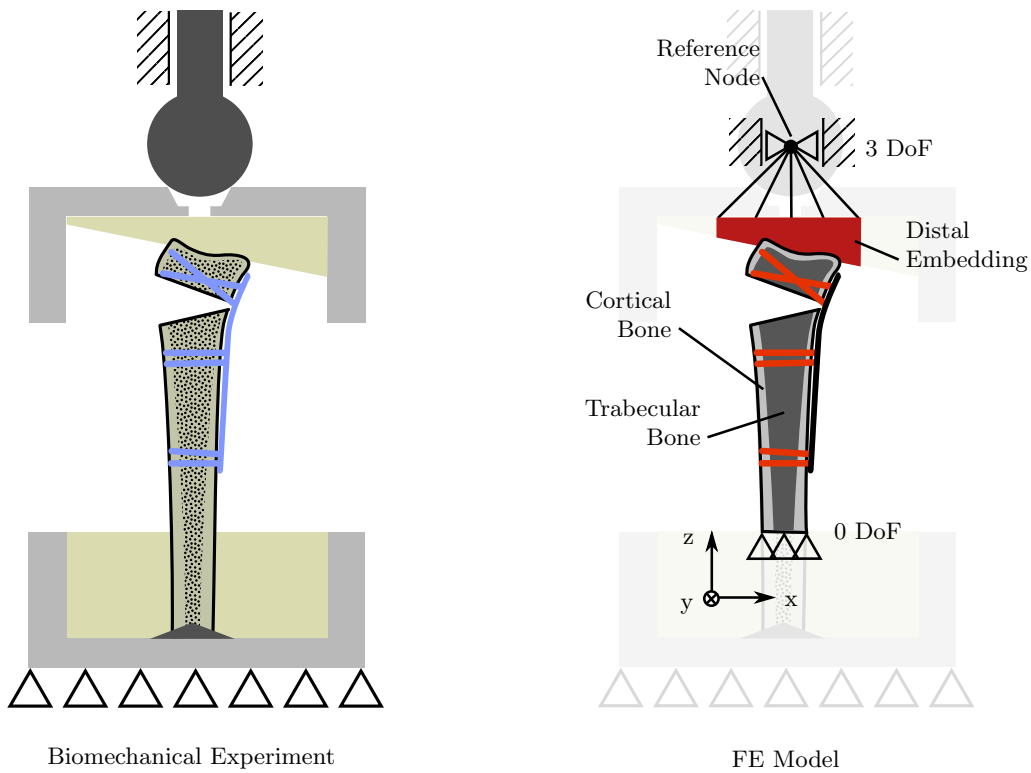


Figure 2.10: Schematic comparison of experimental setup and FE model

Component	Subcomponent	Material Model	Symmetry	Homogeneity
Bone	Spongiosa	Visco-plastic, damage	Orthotropic	Inhomogeneous
	Cortex	Visco-plastic, damage	Isotropic	Inhomogeneous
Implant	Plate	Linear elastic	Isotropic	Homogeneous
	Screws	Linear elastic	Isotropic	Homogeneous
Embedding	-	Linear elastic	Isotropic	Homogeneous

Table 2.1: Overview of the material modelling approach

Component	Subcomponent	Interface			
		Bone	Plate	Screws	Embedding
Bone	Spongiosa	-	No contact	Bonded	Bonded
	Cortex	-	No contact	Bonded	Bonded
Implant	Plate	No contact	-	Bonded	-
	Screws	Bonded	Bonded	-	-
Embedding	-	Bonded	No contact	-	-

Table 2.2: Modelling of the material interfaces

The boundary conditions were chosen similar to the biomechanical experiments. Proximally, movements of the bone were constrained in all spatial directions. The distal ball joint was simulated by defining a kinematic constraint: A reference node was positioned at the center of the steel sphere and coupled to the most distal nodes of the distal embedding with six degrees of freedom (DoF). Translational DoFs in x- and y-direction of the reference node were constrained while rotations were unconstrained. Load was imposed as a displacement of the reference node along the z-axis.

The generation of the FE models was based on HR-pQCT data of the intact, QCT data of the prepared specimen, template geometries representing the implant, embedding and fracture gap and the experimental boundary conditions. The data flow of the model generation process is displayed in Figure 2.11. HR-pQCT and QCT data were processed to obtain the bone geometry in each image coordinate system. Semi-automatic registration was performed on the bones to find the transformation between the two coordinate systems. The template geometries were aligned as indicated in the QCT image, transformed into the HR-pQCT coordinate system and combined with the HR-pQCT image containing segmented trabecular and cortical bone regions. The resulting combined 3D image was meshed and transformed to be aligned similarly to the biomechanical experiments. Bone material data was extracted from the HR-pQCT image and mapped to the FE mesh. The final FE model was then generated by imposing the experimental boundary conditions.

Image processing, mesh generation, and FE model assembly were performed in MedTool (Dr. Pahr Ingenieure e.U., Pfaffstätten, Austria), which is a script management tool developed at the Technical University of Vienna. The open source 3D modelling software Blender (Blender Foundation, Amsterdam, Netherlands) was used to perform the registration and to generate and align the template geometries. Model solving and postprocessing were done in Abaqus (Dassault Systèmes, Vélizy-Villacoublay, France).

The following sections describe the whole model generation procedure in more detail. Sections are structured in accordance to Figure 2.11 and present the QCT and HR-pQCT image processing (A), QCT to HR-pQCT registration (B), modelling in Blender (C), generation of the combined image (D) and assembling the FE model (E). Solving of the model and postprocessing of the results will be addressed in the final section.

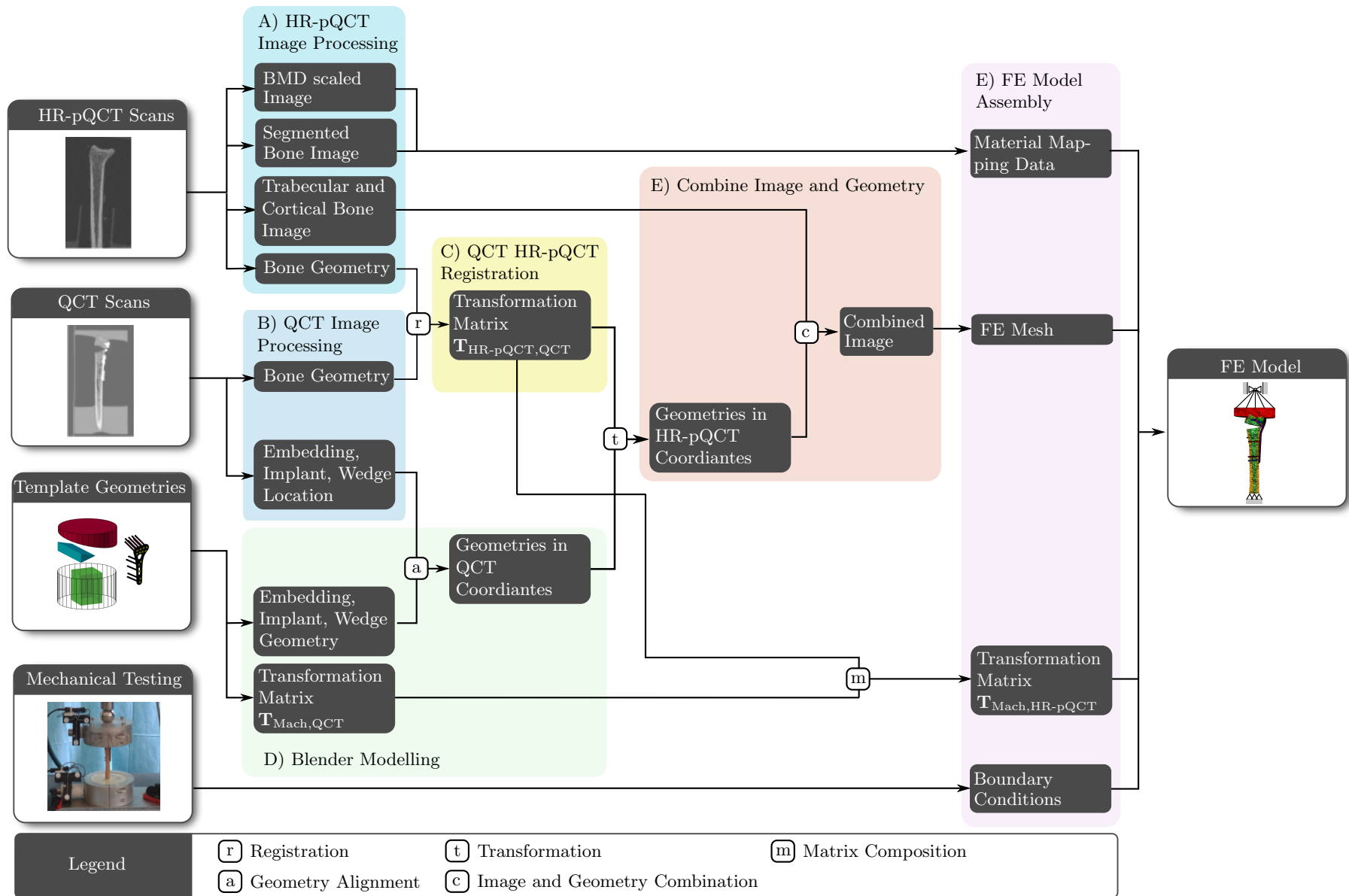


Figure 2.11: Data flow in the FE model generation

2.2.1 QCT Image Processing

The QCT data was used to generate surfaces of the bone, implant as well as the proximal and distal embedding. Segmentation, i.e. labelling of voxels, was necessary to identify all of these components and to create a representation of their boundary. All these steps are explained in the remainder of this section.

A Discovery CT750HD scanner (GE Healthcare GmbH, Solingen, Germany, tube current: 260mA, tube potential: 140kVp) was used to obtain QCT images of the prepared samples with an anisotropic voxel size of approximately 0.2x0.2x0.63mm and dimensions 512x512x250. Figure 2.12 shows the grey value distribution and 3D representation of an exemplary QCT image. A distinct peak was observed for the implant core, while bone and embedding material could not be separated clearly from each other.

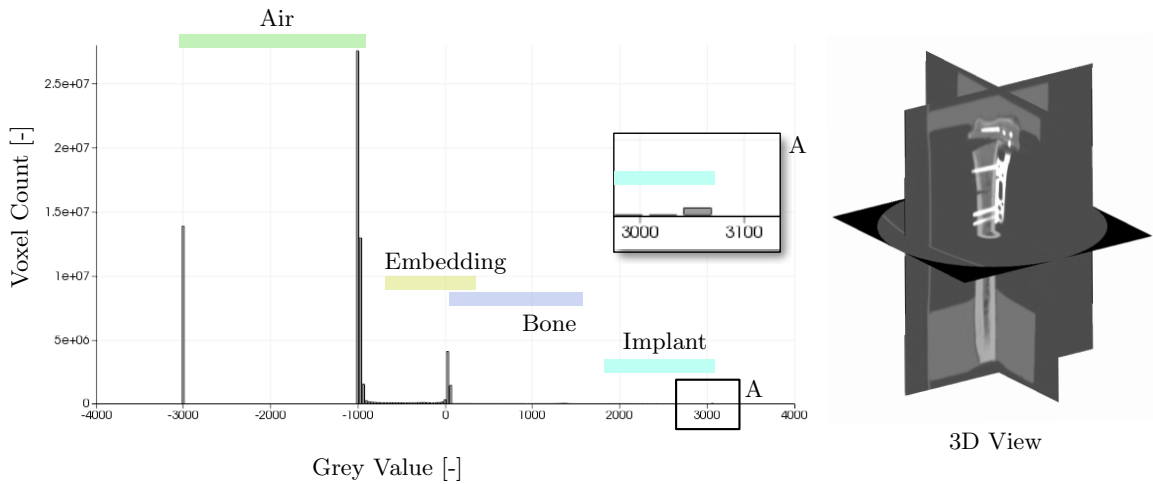


Figure 2.12: Exemplary QCT image histogram and 3D representation

Prior to segmentation, the 3D image was masked to exclude components other than the prepared specimen such as the scanning desk. This mask was created by applying a fixed threshold, morphological filters and an island removal algorithm which deletes floating voxels. This procedure ensured that small, unconnected structures and noise were discarded while small holes within the mask were closed.

The further QCT image processing is shown in Figure 2.13. The segmentation of the implant was performed with a fixed threshold based on the histogram data. More steps were required to label the bone voxels. First, a fixed threshold was applied which covered single voxels of the embedding, large regions of the bone and the whole implant. A morphological closing filter was applied to ensure that most of the regions of the bone were connected. The segmented implant was then used as a mask and a morphological opening filter was used to discard floating voxels and narrow voxel regions. Finally, a custom algorithm was applied to fill remaining holes of trabecular bone regions. The algorithm is based on region growing and morphological filters and is described in more detail by Pahr et al. [56].

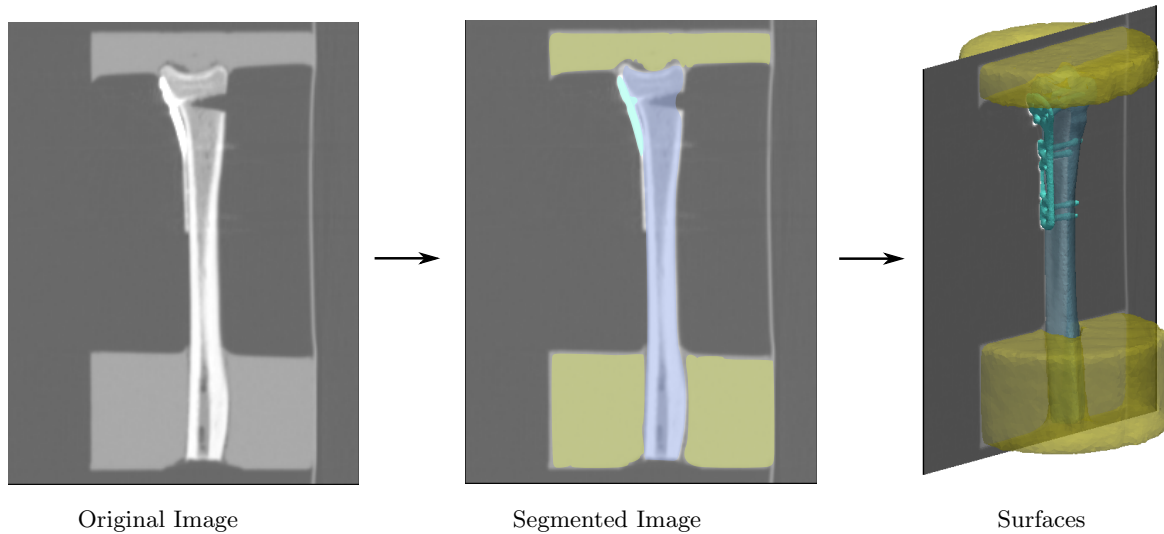


Figure 2.13: QCT image segmentation and surface generation

The embedding was then identified by masking the image with both bone and implant regions. Separation of distal and proximal embedding was performed with an island removal filter, which keeps only the largest connected region of voxels in the image, i.e. the proximal embedding. The distal embedding could then be found by subtracting the image of the proximal from the image containing both embeddings.

The triangulated surfaces of all labelled regions were subsequently generated with the 3D meshing algorithm of the Computational Geometry Algorithms Library (CGAL) as implemented in MedTool. A facet distance of 0.5mm and a cell size of 1mm were used as meshing parameters. The facet distance controls the quality of the mesh approximation to the original boundary and the cell size limits the circumsphere of the generated elements [57]. Following surface meshing, Taubin smoothing, as implemented in MedTool, was applied to all surfaces to reduce noise.

2.2.2 HR-pQCT Image Processing

Processing of the HR-pQCT data was required to obtain three different 3D images for each specimen: A BMD scaled bone image, a binary image of the segmented bone and an image containing separated regions of trabecular and cortical bone. Additionally, surface meshes of the outer bone needed to be generated for registration with the QCT derived bone surface.

The HR-pQCT scans were conducted in an XtremeCT device (Scanco Medical AG, Brüttisellen, Switzerland, tube current: $900\mu\text{A}$, tube potential: 60kVp) and images were reconstructed with an isotropic voxel size of 0.082mm and dimensions 1536x1536x1617. The images were cropped to the size of an automatically computed, padded bounding box prior to processing in order to reduce computational time.

The XtremeCT was calibrated such that the voxel grey values (GV) linearly relate to the BMD in mg hydroxyapatit (HA) per cubic centimetre. Accounting for the device specific scaling factor and the scan specific slope and intercept of the calibration curve, the BMD values were computed as follows:

$$\text{BMD} = \frac{\text{GV}}{8192} \cdot 1447 - 353.1 \quad (2.1)$$

The range of BMD values was then limited to a range of -100 and 1400 mgHA/cm³ to exclude noise and artifacts [58]. The BMD values will be used to compute the bone volume fraction in later step (see Section 2.2.6) and serve as an input to the material model. Figure 2.14 shows the BMD and segmented bone image exemplary for one specimen.

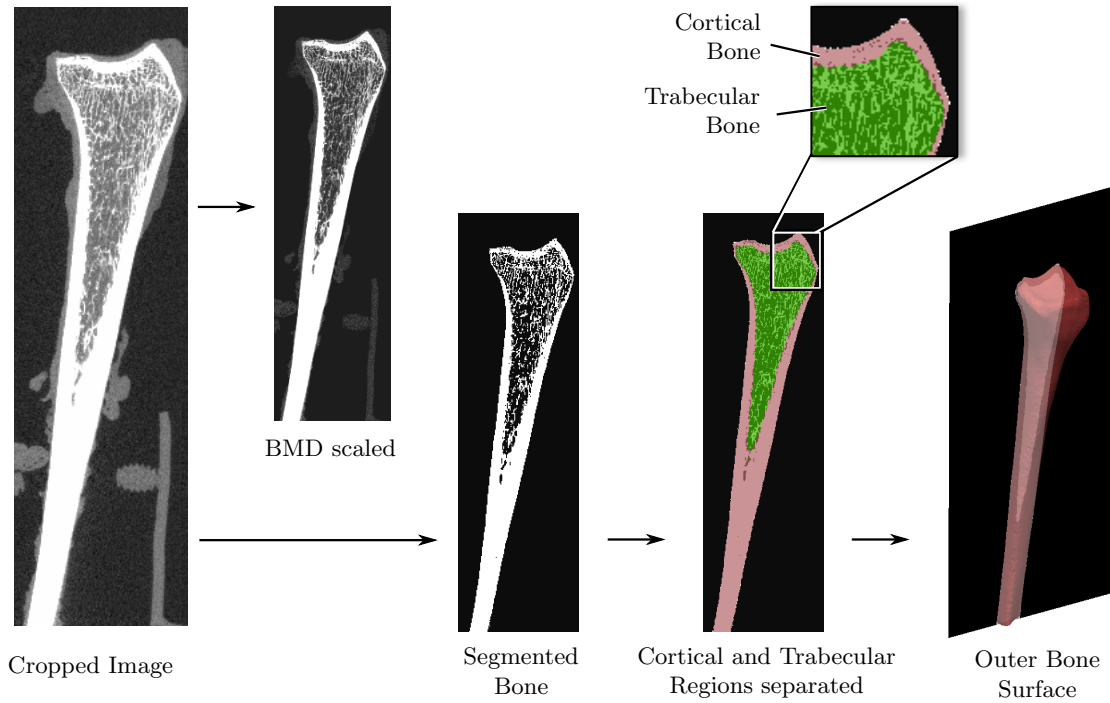


Figure 2.14: HR-pQCT image processing and bone surface generation

Segmentation of the bone including the trabecular structure was performed automatically on the original HR-pQCT image following a method used by the HR-pQCT device manufacturer Scanco. In brief, a Laplace-Hamming filter was applied for edge detection, followed by a fixed grey value cut off, threshold segmentation and an island removal filter.

The resulting image was used to label cortical and trabecular bone regions. First, a morphological filter was applied to close small pores of the cortical shell. Second, the custom filling algorithm of MedTool [56] was used to identify cortical and trabecular bone regions. Third, morphological opening, island removal and closing filters were applied to remove small bone fragments contained in the soft tissue surrounding the bone and for smoothing the 3D image.

Prior to surface generation, the 3D image was expanded by adding voxel layers to account for the embedding and implant geometry which would be inserted in subsequent processing steps (see Section 2.2.5). The outer surface of the segmented bone was then meshed following the same procedure as for the QCT images. CGAL was used to generate the surfaces with a facet distance of 0.5mm and a cell size of 1mm and a Taubin filter was applied for smoothing and noise reduction.

2.2.3 QCT to HR-pQCT Registration

In order to combine the information contained in the HR-pQCT and QCT data it was necessary to find a transformation matrix which relates corresponding coordinate systems. A surface based, semi-automatic registration approach was chosen to find this transformation based on the generated bone geometries.

Challenges in the registration of the presented data included the arbitrary initial alignment and limited similarity of the geometries generated from the QCT and HR-pQCT images (see Figure 2.15). The bone surface generated from QCT differed from the HR-pQCT derived surface particularly due to the fracture gap and inserted screws. The iterative closest point algorithm (ICP) is a standard method for surface based registration [59] and was chosen for registering the bone geometries as it is capable of matching surfaces which are only partially overlapping [60]. ICP based registration works in two main steps [61]: First, the algorithm establishes node correspondences by finding the closest node of a target surface for each node of a source surface. Second, the mean squared distance between all node pairs is minimized by applying an optimal transformation to the source surface. These steps are iterated until a convergence criterion, e.g. a threshold of the mean distance, is met. A major drawback of the ICP algorithm is that it is a local optimization method, such that pre-alignment of the geometries is required [62].

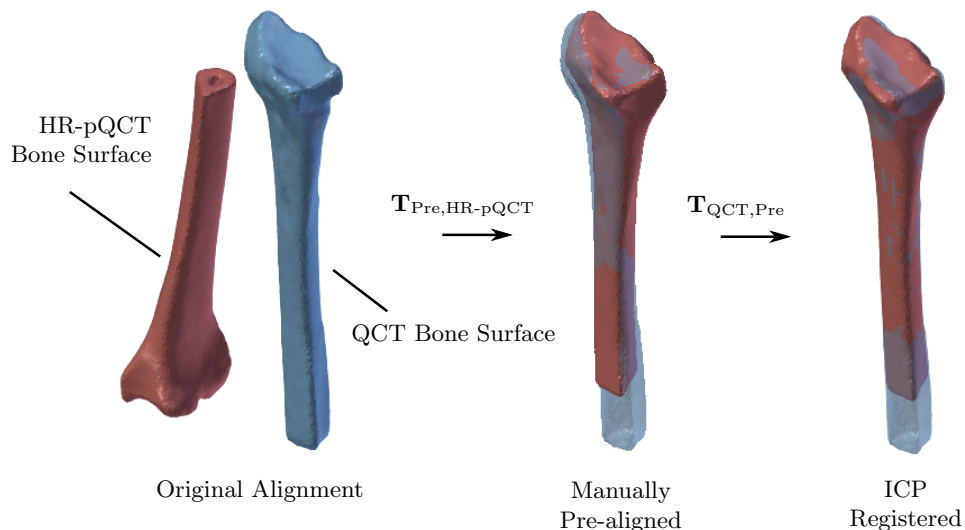


Figure 2.15: Semi-automatic registration of the QCT and HR-pQCT derived bone surfaces

In order to pre-align the bone geometries, the ICP implementation of the visualization toolkit (VTK) was integrated into Blender using a custom Python script. Both bone geometries were then imported, manually pre-aligned and registered with the ICP algorithm (see Figure 2.15). Only rigid transformations were allowed to exclude skew or scaling. A maximum of 100 iterations and a threshold mean distance of 0.01mm were chosen.

After the registration, a transformation matrix \mathbf{T} was computed which allows to apply both a rotation and translation to a vector in a single operation [63]. The 4x4 transformation matrix is defined based on the 3x3 rotation matrix \mathbf{R} and a 3x1 translation vector \mathbf{t} as follows:

$$\mathbf{T} = \begin{bmatrix} \mathbf{R} & \mathbf{t} \\ 0 & 1 \end{bmatrix} \quad (2.2)$$

A requirement for its application is the transition of each vector from Cartesian to homogeneous coordinates:

$$\begin{bmatrix} x_1 \\ x_2 \\ x_3 \end{bmatrix} \rightarrow \begin{bmatrix} x_1 \\ x_2 \\ x_3 \\ 1 \end{bmatrix} \quad (2.3)$$

Given a vector \mathbf{x} in homogeneous coordinates, the transformation from coordinate system \mathcal{A} to system \mathcal{B} is then defined by $\mathbf{T}_{\mathcal{B},\mathcal{A}}$ as follows:

$$\mathbf{x}_{\mathcal{B}} = \mathbf{T}_{\mathcal{B},\mathcal{A}} \mathbf{x}_{\mathcal{A}} = (\mathbf{T}_{\mathcal{A},\mathcal{B}})^{-1} \mathbf{x}_{\mathcal{A}} \quad (2.4)$$

Using the above notation, the transformation matrix $\mathbf{T}_{\text{HR-pQCT},\text{QCT}}$ was computed from the pre-alignment and registration which transforms a vector from QCT to the HR-pQCT coordinate system:

$$\mathbf{T}_{\text{HR-pQCT},\text{QCT}} = (\mathbf{T}_{\text{QCT},\text{HR-pQCT}})^{-1} = (\mathbf{T}_{\text{QCT},\text{Pre}} \mathbf{T}_{\text{Pre},\text{HR-pQCT}})^{-1} \quad (2.5)$$

In single cases, QCT surfaces could not be obtained in sufficient quality such that the ICP algorithm delivered poor results. Manual correction was applied in cases of obvious misalignment between the bones.

2.2.4 Blender Modelling

Blender was not only used for semi-automatic registration of the scanning modalities but also to generate and position the implant, fracture gap and embedding geometries. As all of these components needed to be aligned multiple times, a template file was generated which allowed fast manipulation and adaptation of all geometries.

The general structure of the Blender template file is outlined in Figure 2.16. Four objects were modelled: The implant, the distal embedding, the proximal embedding and a wedge which represented the fracture gap.

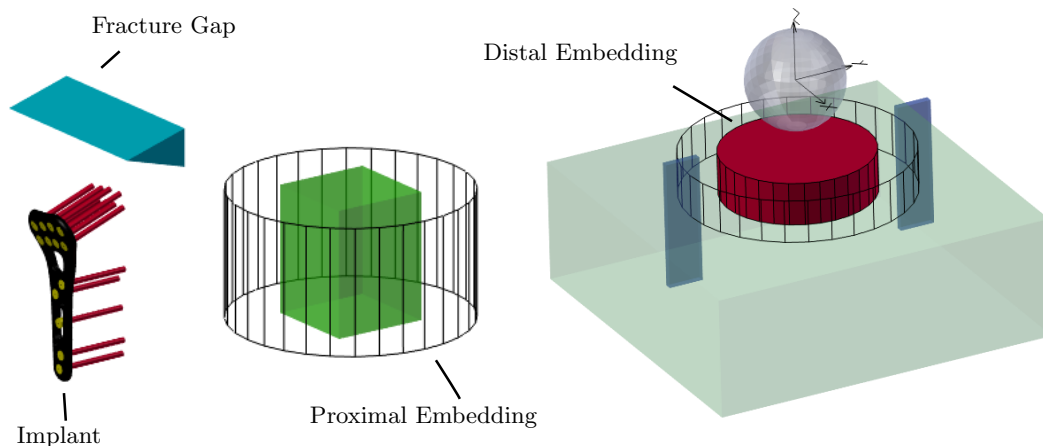


Figure 2.16: Overview of the four components of the Blender template file

The implant consisted of the implant plate, screw heads and screw shafts (see Figure 2.17). The geometry of the plate was obtained from the manufacturer and imported into blender. Screw heads were modelled in Blender as skewed cylinders which entirely fill the holes of the implant plate. They were connected to the plate by a parenting relation such that the screw heads would follow any movement imposed on the plate.

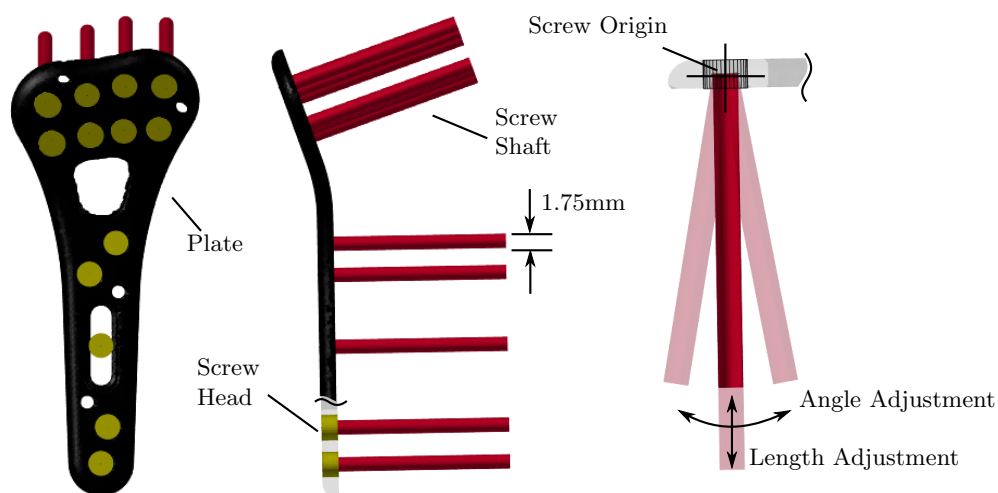


Figure 2.17: Implant template modelled in Blender

The screw shafts were drawn in Blender as cylinders with a diameter of 1.75mm, which was consistent with the measured core diameter of the locking screws. The origin of the screw shafts was positioned at the center of the implant plate holes and a parenting relation was introduced similarly to the screw heads. As a result, the implant plate was free to move into any position while the screw heads and shafts would track the movement. Individual screw shaft orientations could then be obtained by rotations around their origin. The length of the shaft was adjustable by scaling the geometry in the local coordinate system.

The fracture gap was modelled in Blender as a simple wedge with an opening of 10mm, a depth of 20mm and a width of 60mm. Manipulation of the wedge vertices allowed for adaptation to the specimen specific fracture gap. A cylinder of 40mm height and 75mm diameter represented the proximal embedding. As the embedding would not be contained in the final image but rather used for cutting the bone proximally, a smaller, cuboid cutting geometry was connected to the embedding by a parenting relation. Fracture gap and proximal embedding modelling is displayed in Figure 2.18.

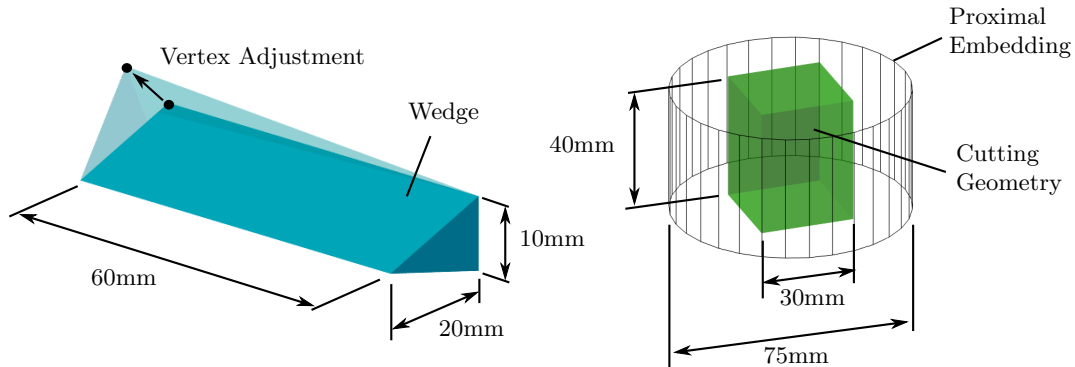


Figure 2.18: Fracture gap and proximal embedding as modelled in Blender

The distal embedding was also represented by a cylinder but reduced to a diameter of 50mm (see Figure 2.19). The proximal tilt of the embedding was modelled by boolean subtraction of a cuboid geometry. Distally, the steel sphere used for the load transfer in the biomechanical tests was modelled and positioned as measured in the experimental setup. A coordinate system was placed in the center of the sphere. Radial and ulnar alignment plates were attached to the distal embedding geometry to ensure uniform alignment of the coordinate system with respect to the implant plate. This coordinated system will be referred to as the machine coordinate system in the following as the specimens were aligned similarly in the testing machine of the experimental setup.

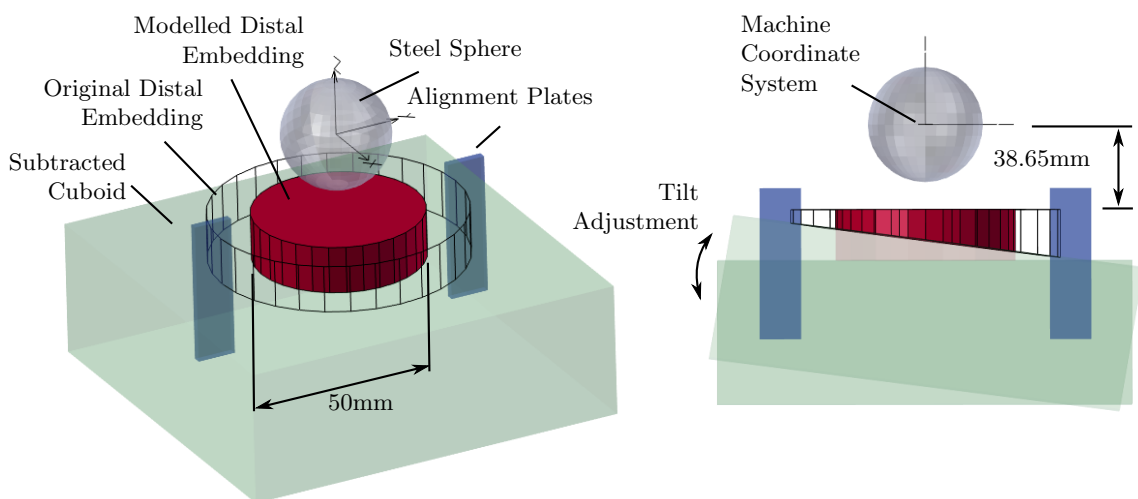


Figure 2.19: Distal embedding modelled in Blender

The completed Blender template file was then used to adapt all components to the surfaces generated from the QCT images (see Figure 2.20). First, the fracture gap was manually adapted by manipulating the wedge vertices. Second, the implant plate was registered to the QCT implant surface using the ICP algorithm implementation described in Section 2.2.3 and the screw orientations and lengths were manually modified. Third, the proximal embedding was automatically registered to the QCT derived surface. Finally, the distal embedding was manually positioned and modified such that the proximal tilt of the embedding was captured and the radial and ulnar plate were aligned coplanar with the implant plate. All Blender geometries were then exported individually as triangulated surfaces.

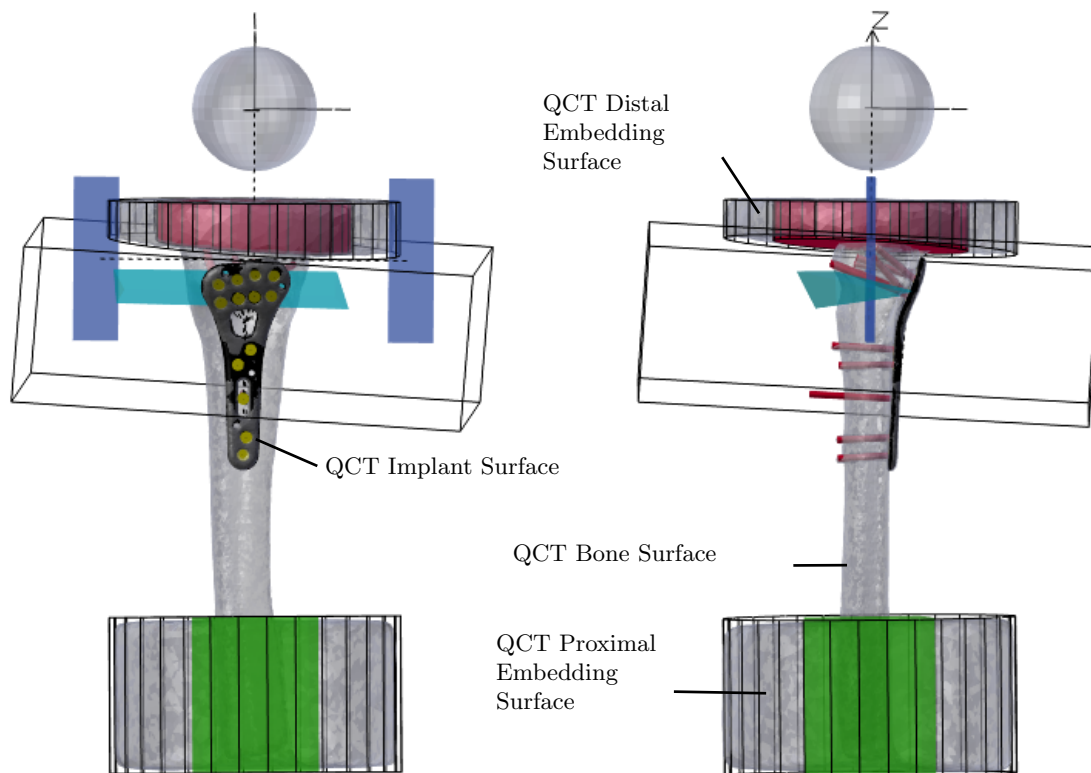


Figure 2.20: Alignment of the Blender geometries to the QCT derived surfaces

Additionally, the transformation matrix $\mathbf{T}_{\text{Mach},\text{QCT}}$, which transforms points of the QCT coordinate system to the machine coordinate system, was saved for each specimen.

2.2.5 Combining Image and Geometries

A combined high resolution image containing bone regions, implant and embedding was needed as a basis for generating the FE mesh. For this purpose, QCT-aligned template geometries were transformed into the HR-pQCT coordinate system and inserted into the HR-pQCT derived image of cortical and trabecular bone regions. Details are provided in the remainder of this section.

Combining the 3D image with the surfaces was conducted in three steps: First, the surfaces were transformed into the HR-pQCT coordinate system using the transformation matrix $\mathbf{T}_{\text{HR-pQCT},\text{QCT}}$. The transformed surfaces were then filled with tetrahedral elements using the finite element mesh generator Gmsh. Third, a custom algorithm implemented in MedTool was used to find voxels with centroids inside the mesh elements. In brief, the algorithm computes the signed normal distances of a voxel centroid to the the four planes bounding the tetrahedron. If all signs coincide, the voxel lies inside the tetrahedron and is assigned a given grey value. This procedure is repeated for all tetrahedra.

An exemplary image combined with geometries is displayed in Figure 2.21. The shaft of the bone was cut by replacing all voxels contained in the cutting geometry of the proximal embedding with zero. Similarly, voxels inside the wedge were set to zero to simulate the fracture gap. The distal embedding was created as follows: First, the distal embedding geometry was inserted into the image. Second, a fill operation was performed to avoid gaps between embedding and the articular concavity. Third, the embedding image was masked with the bone image, cleaned from floating voxels and finally combined with the trabecular and cortical bone image.

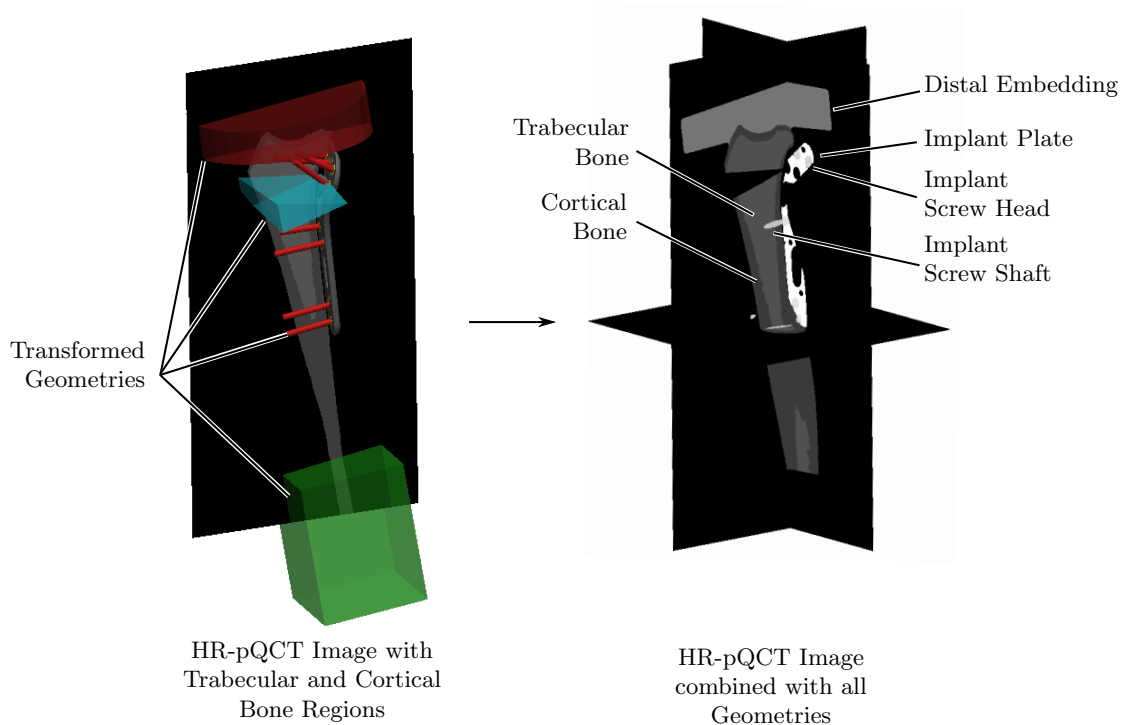


Figure 2.21: Generation of the combined image

The screw shaft geometries were then inserted into the image with a screw-individual grey value. Screw heads and plate were inserted and combined in an empty image and masked with the bone image. This step was necessary to avoid implant protrusion into the bone material in case of misalignments. The masked implant plate and screw head image was then combined with the image containing trabecular and cortical bone, screw shafts and the distal embedding.

2.2.6 FE Model Assembly

In order to generate the FE model it was necessary to generate a mesh, assign the material properties, and to impose the boundary conditions. Additionally, connector elements were introduced at the screw-plate interface to quantify section forces at each screw. All of these steps will be explained in the remainder of this section.

Tetrahedral meshes were generated from the combined 3D images using CGAL. The generated mesh contained one element set for each grey value in the image. The meshing algorithm allows to define several parameters which influence the mesh quality [57]. Of all available parameters, the facet distance and cell size have the most pronounced impact on the generated mesh. The facet distance is used to set an upper bound for the approximation error of the mesh to the original boundaries, whereas the cell size is used to set the maximum circumradius of the tetrahedra. A facet distance of 0.12mm and a cell size of 2mm was chosen for generating the meshes of the bone-implant system following convergence tests on a single specimen. The mesh quality was then improved by applying both global and local optimizers of CGAL which either seek to minimize a global energy criterion or to improve the quality of single tetrahedra. The chosen sequence of optimizers were Lloyd, Perturb, and Exude. The generated mesh is displayed in Figure 2.22.

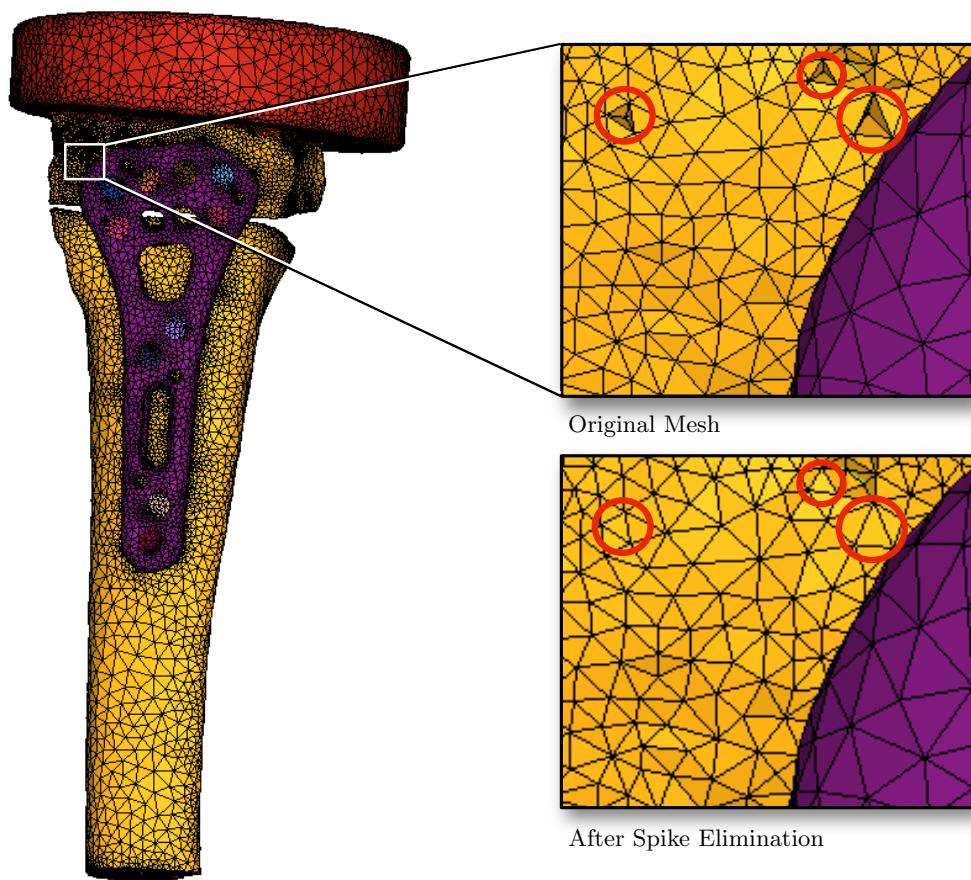


Figure 2.22: Generated mesh and improvement by spike elimination

A limitation of the CGAL meshing procedure is its accuracy with respect to the original geometrical boundary, i.e. the fidelity. In particular, elements at an element set boundary might be assigned to the wrong domain (see Figure 2.22). Further decreasing the facet distance would diminish the problem of inaccuracy but result in a drastically increased element count. Another approach was pursued as a trade off between element count and fidelity: The whole image was meshed including the surrounding air of the bone-implant system. A custom Python script was then used to identify spike elements of each element set, i.e. elements with a node that is not shared with any other element of the observed element set. The facet neighborhood was then computed to create a list of element sets the spike element could belong to. Majority voting was used to assign the spike element to a new element set. Following spike elimination, the elements and nodes constituting the surrounding air were deleted. Using this approach it was possible to eliminate both spikes and small indents at the element set boundaries of the mesh.

All first-order tetrahedral elements (C3D4) were subsequently converted to second order elements (C3D10). The resulting mesh contained the bone, the implant and the embedding. All of these components were fully bonded at the nodes of the element set boundary. This type of bonding was reasonable for the bone-embedding and bone-screw interface but was undesired at the bone-implant plate interface. Separation of the corresponding element sets was, therefore, conducted by duplicating shared nodes with a custom Python script.

Bone material data was then assigned to the generated mesh with a material mapping algorithm developed by Pahr et al. [56] and implemented in MedTool. In brief, the algorithm computes a spatial background grid and estimates the ratio of bone volume to total volume (BV/TV) as well as the orientation and anisotropy (fabric tensor) of the bone material contained in a spherical volume of interest around each point of the grid. Subsequently, the FE mesh is superimposed by the grid and each element is assigned a linearly interpolated BV/TV and fabric tensor based on the location of the element centroid with respect to the grid points. The BV/TV of each volume of interest was computed based on the BMD scaled HR-pQCT images and the device specific calibration law reported by Luisier et al. [58]:

$$\text{BV/TV} = -1.58^{-12} \text{BMD}^4 + 2.03^{-9} \text{BMD}^3 - 4.74^{-7} \text{BMD}^2 + 1.01^{-3} \text{BMD} \quad (2.6)$$

In practice, BV/TV and fabric tensor were computed based on a grid with 3.5mm spacing and 7.5mm diameter spheres. BMD scaled and segmented bone images of section 2.2.2 were masked with trabecular and cortical regions and served as an input for the material mapping algorithm. BMD scaled and masked images were used to derive the average BV/TV in the volume of interest of both cortex and spongiosa. Fabric tensors were computed based on the mean intercept length method (MIL) from the masked and segmented images only for trabecular bone and normalized by their trace. The input data and results of the material mapping are shown in Figure 2.23 for a single specimen. Orientations are indicated by the direction and magnitude of the maximum elastic modulus E_{max} of each element.

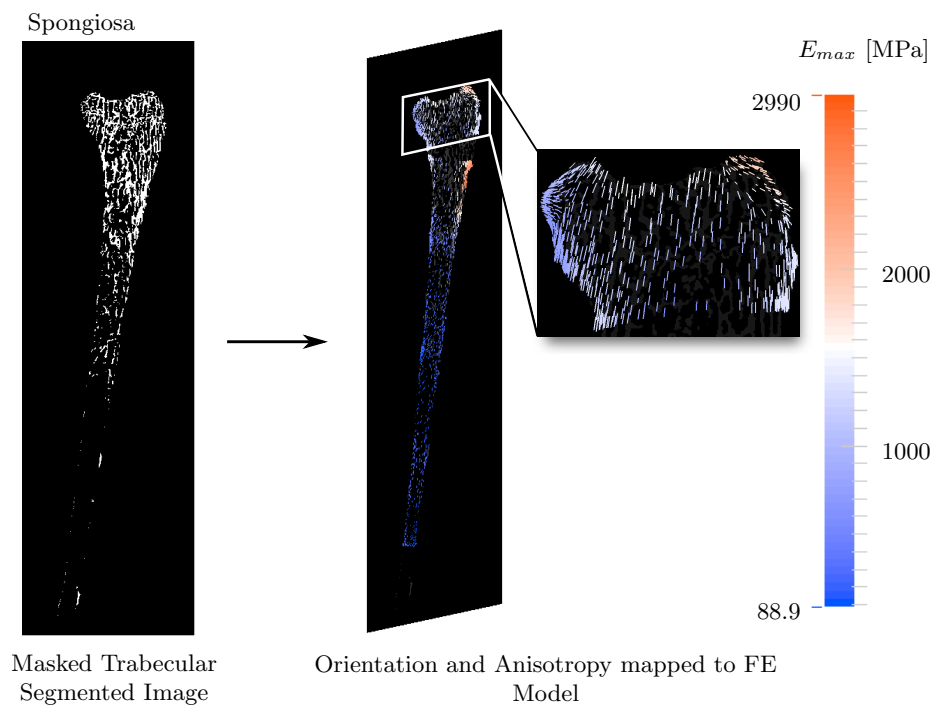
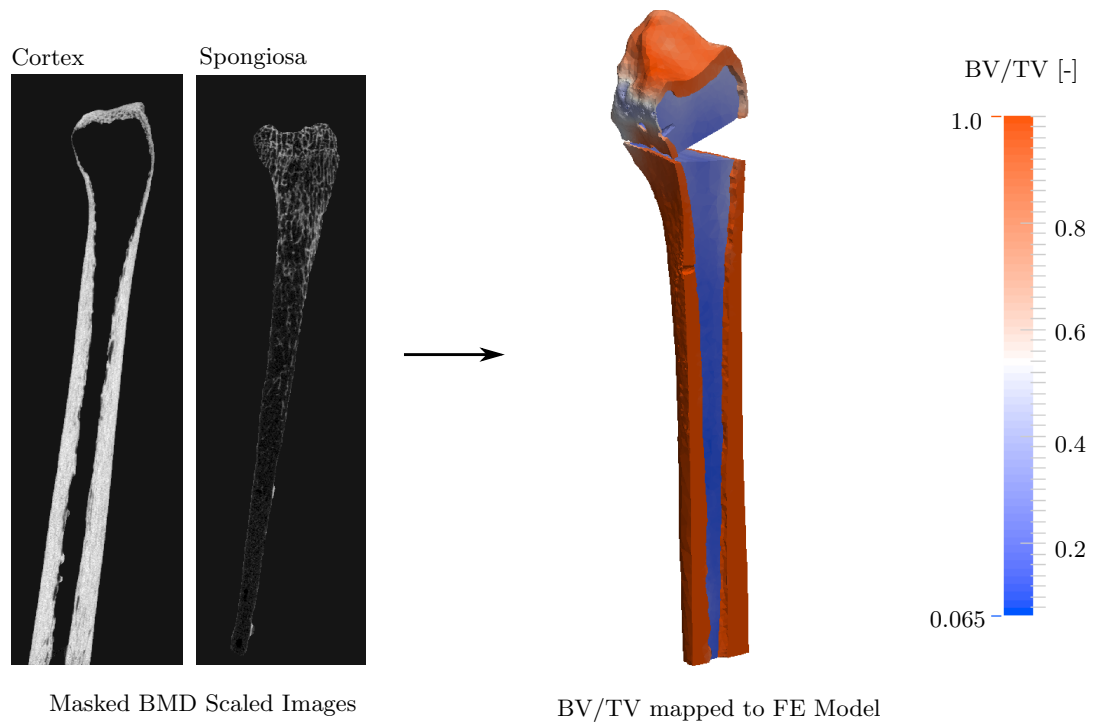


Figure 2.23: Bone material mapping for an exemplary specimen

The element specific BV/TV and fabric tensor were then used as parameters for a viscoplastic damageable material model as proposed by Schwiedrzick et al. [64]. In this model, damage due to micro-crack formation is represented by an internal scalar damage variable D , which decreases all elements of the stiffness tensor \mathbb{S} and ranges from 0 (intact) to 1 (complete failure). D is assumed to be a function of the cumulated plastic strain κ . The free energy potential for the material model is defined as follows:

$$\Psi(\mathbf{E}, \mathbf{E}^p, \kappa) = \frac{1}{2}(1 - D(\kappa))(\mathbf{E} - \mathbf{E}^p) : \mathbb{S}(\mathbf{E} - \mathbf{E}^p) \quad (2.7)$$

In the above formula, \mathbf{E} denotes the total strain tensor and \mathbf{E}^p is the inelastic or plastic strain tensor. The orthotropic compliance tensor \mathbb{C} is the inverse of the stiffness tensor \mathbb{S} and defined by 9 independent material constants. In matrix notation, the compliance tensor \mathbb{C} reads:

$$\mathbb{C} = \mathbb{S}^{-1} = \begin{bmatrix} \frac{1}{E_1} & -\frac{\nu_{12}}{E_1} & -\frac{\nu_{13}}{E_1} & 0 & 0 & 0 \\ -\frac{\nu_{21}}{E_2} & \frac{1}{E_2} & -\frac{\nu_{23}}{E_2} & 0 & 0 & 0 \\ -\frac{\nu_{31}}{E_3} & -\frac{\nu_{32}}{E_3} & \frac{1}{E_3} & 0 & 0 & 0 \\ 0 & 0 & 0 & \frac{1}{2G_{12}} & 0 & 0 \\ 0 & 0 & 0 & 0 & \frac{1}{2G_{13}} & 0 \\ 0 & 0 & 0 & 0 & 0 & \frac{1}{2G_{23}} \end{bmatrix} \quad (2.8)$$

E_i , ν_{ij} and G_{ij} are the elastic moduli, Poisson ratios and shear moduli, respectively and ':' is the double contraction operation. Based on the eigenvalues of the fabric tensor m_i , the BV/TV ρ and five constants E_0 , ν_0 , G_0 , k and l , they can be computed as follows:

$$\begin{aligned} E_i &= E_0 \rho^k m_i^{2l} \\ G_{ij} &= G_0 \rho^k m_i^l m_j^l \\ \nu_{ij} &= \nu_0 \frac{m_i^l}{m_j^l} \end{aligned} \quad (2.9)$$

Compact bone is assumed to be isotropic such that m_i equal 1. In this case, the material compliance is fully defined by ρ , E_0 , ν_0 and k . The constants required to define the elastic behavior of trabecular and compact bone are displayed in Table 2.3 and adapted from Gross et al. [65] and Cowin et al. [66].

	E_0 [MPa]	ν_0 [-]	G_0 [MPa]	k [-]	l [-]
Spongiosa	9995	0.2278	3361	1.62	1.1
Cortex	19327	0.3434	-	1.63	-

Table 2.3: Elastic material constants of bone

The elastic region is bound by an anisotropic yield surface $Y(\mathbf{S})$ in stress space defined as:

$$Y(\mathbf{S}) = \sqrt{\mathbf{S} : \overline{\mathbf{F}}\mathbf{S}} + \mathbf{F} : \mathbf{S} - 0.7 - 0.3r(\kappa) = 0 \quad (2.10)$$

\mathbf{F} and \mathbb{F} are symmetric second and fourth order tensors which describe the origin, as well as the shape and orientation of the yield criterion, whereas $r(\kappa)$ determines the material behavior beyond the yield point. \mathbf{S} denotes the stress tensor. \mathbf{F} is defined as follows:

$$\mathbf{F} = -\frac{1}{\rho^p} \frac{\sigma_0^+ - \sigma_0^-}{2\sigma_0^+ \sigma_0^-} \begin{bmatrix} \frac{1}{m_1^{2q}} & 0 & 0 \\ 0 & \frac{1}{m_2^{2q}} & 0 \\ 0 & 0 & \frac{1}{m_3^{2q}} \end{bmatrix} \quad (2.11)$$

With

$$\sigma_0 = \frac{\sigma_0^+ + \sigma_0^-}{2\sigma_0^+ \sigma_0^-} \quad (2.12)$$

\mathbb{F} is represented by:

$$\mathbb{F} = \frac{1}{\rho^{2p}} \begin{bmatrix} \frac{\sigma_0^2}{m_1^{4q}} & -\frac{\zeta_0 \sigma_0^2}{m_1^{2q} m_2^{2q}} & -\frac{\zeta_0 \sigma_0^2}{m_1^{2q} m_3^{2q}} & 0 & 0 & 0 \\ -\frac{\zeta_0 \sigma_0^2}{m_1^{2q} m_3^{2q}} & \frac{\sigma_0^2}{m_2^{4q}} & -\frac{\zeta_0 \sigma_0^2}{m_2^{2q} m_3^{2q}} & 0 & 0 & 0 \\ -\frac{\zeta_0 \sigma_0^2}{m_1^{2q} m_3^{2q}} & -\frac{\zeta_0 \sigma_0^2}{m_2^{2q} m_3^{2q}} & \frac{\sigma_0^2}{m_3^{4q}} & 0 & 0 & 0 \\ 0 & 0 & 0 & \frac{1}{2(\tau_0 m_1^q m_2^q)^2} & 0 & 0 \\ 0 & 0 & 0 & 0 & \frac{1}{2(\tau_0 m_1^q m_3^q)^2} & 0 \\ 0 & 0 & 0 & 0 & 0 & \frac{1}{2(\tau_0 m_2^q m_3^q)^2} \end{bmatrix} \quad (2.13)$$

Thus, the yield surface is derived from the volume fraction ρ , the fabric eigenvalues m_i and five constants: σ_0^+ , σ_0^- and τ_0 are the uniaxial tension, uniaxial compression and the shear strength, respectively. p is the power law exponent and ζ_0 is a biaxial interaction parameter which determines the shape of the criterion.

For the isotropic case, τ_0 is computed from σ_0^+ , σ_0^- and ζ_0 as follows:

$$\tau_0 = \left(\frac{1}{\sigma_0^+} + \frac{1}{\sigma_0^-} \right) \sqrt{\frac{2}{1 + \zeta_0}} \quad (2.14)$$

Yield constants for both trabecular and cortical bone are shown in Table 2.4 and derived from Wolfram et al. [67] and Cowin et al. [66], respectively.

	σ_0^+ [MPa]	σ_0^- [MPa]	ζ_0 [-]	τ_0 [MPa]	p [-]	q [-]
Spongiosa	66.01	98.88	0.2182	41.89	1.69	1.05
Cortex	144.7	234.2	0.4900	-	1.69	-

Table 2.4: Yield material constants of bone

Postyield behavior is governed by $r(\kappa)$ of equation 2.10: Trabecular bone was assumed to exhibit simple softening, whereas exponential hardening was set for cortical bone. Viscoplastic flow is determined by the viscosity η which was set to 10^{-3} MPa·s. Densification due to progressive collapse of trabecular bone is accounted for by the incorporation of a densification function. No densification is assumed in cortical bone.

Additional sets of models were created with isotropic inhomogeneous and isotropic homogeneous bone material properties to assess the relevance of the material modelling approach. Isotropic inhomogeneous models were created similar to the above description but without taking the fabric tensor for trabecular bone into account. Isotropic homogeneous material parameters were chosen in accordance with previous studies on DRF treatments [49, 51]: Constant elastic moduli of 1.4 and 17 GPa were assigned to trabecular and cortical bone, respectively. A Poisson ratio of 0.3 was assumed for both materials.

Implant plate and screws as well as the embedding material were modelled as linear elastic, isotropic and homogeneous materials. The implant plate material is made of unalloyed grade 4 titanium (ASTM F67) with a Young's modulus of 105 GPa and a poisson ratio of 0.37 [68], whereas the screws are made of titanium alloy TiAl6V4 (ASTM F136) with a Young's modulus of 114 GPa and a poisson ratio of 0.34 [69]. The embedding material is a polyurethane casting compound with an elastic modulus of approximately 1.45 GPa [70]. The poisson ratio was not provided by the manufacturer and, therefore, set to 0.3 as used in a previous FE study utilizing a similar embedding material [58].

The resulting mesh and material data were defined in the HR-pQCT coordinate system. To ensure consistent alignment with the biomechanical experiments, the model was transformed by applying the transformation matrices obtained by the registration and from Blender modelling:

$$\mathbf{T}_{\text{Mach,HR-pQCT}} = \mathbf{T}_{\text{Mach,QCT}} \mathbf{T}_{\text{QCT,HR-pQCT}} \quad (2.15)$$

Both mesh nodes and element specific orientations were transformed with $\mathbf{T}_{\text{Mach,HR-pQCT}}$ such that x represented the dorso-volar, y the lateral and z the cranio-caudal axis. The origin of the machine coordinate system indicated the center of the steel sphere of the biomechanical experiment.

In order to resemble the experimental boundary conditions it was necessary to find the most distal and the most proximal nodes of the model. CGAL does, however, not deliver perfectly even boundary surfaces. Thus, a Python script was used to find the most proximal and distal nodes within a predefined tolerance range. In order to exclude interior nodes of the mesh, the boundary of the mesh was computed prior to selecting nodes within this range.

The set of the most proximal nodes was then constrained in all spatial directions (0 DoF). A reference node was generated at the origin of the coordinate system which would represent the center of rotation of the steel sphere. This node was kinematically coupled with 6 DoF to the most distal set of nodes. Translational constraints in x- and y-directions were imposed on the reference node. Loads of the model could then be simulated by prescribing a displacement of the reference node in z-direction. The final, transformed FE model with all boundary conditions of an exemplary specimen is displayed in Figure 2.24.

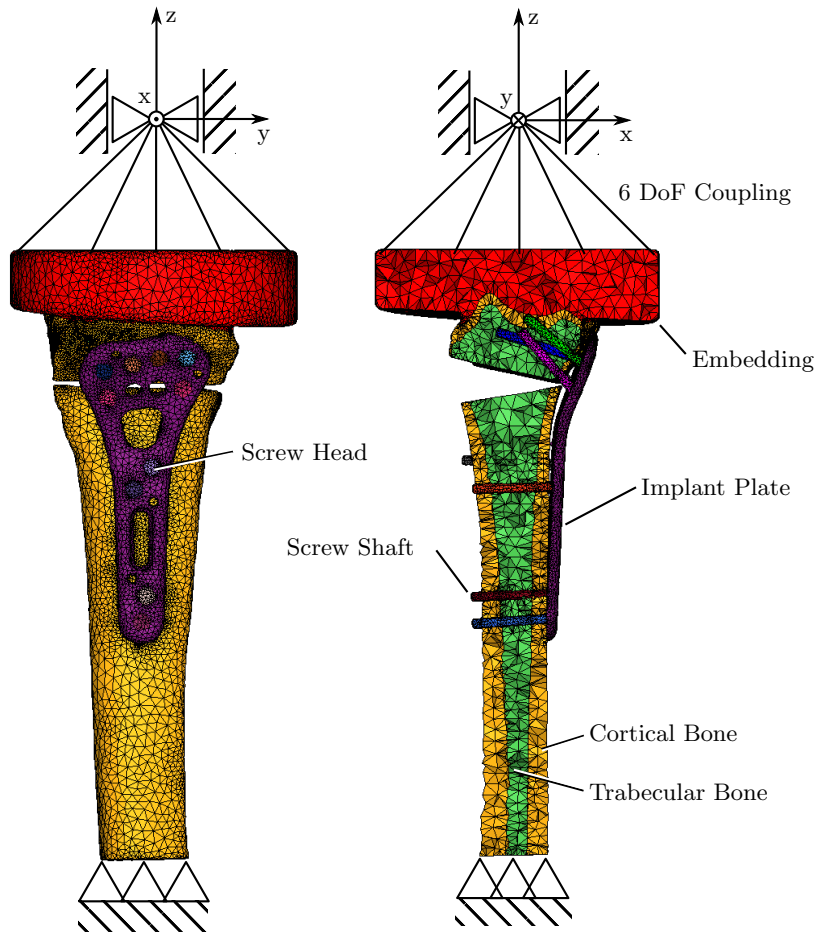


Figure 2.24: An exemplary FE model with boundary conditions

In order to better judge the performance of the implant system, the internal forces and moments acting between the plate and the screws needed to be evaluated. For this purpose, connector elements (CONN3D2) were introduced in between the screw heads and shafts which allow force and moment output in a connector specific coordinate system (see Figure 2.25). The connectors were set up for each screw as follows: First, shared nodes at the screw head and shaft interface were detected and duplicated. Second, two nodes were created at the centroid of these shared nodes. Third, two kinematic couplings were defined for each screw which connect the center node to the set of interface nodes. Fourth, a weld-type connector element was added which constrains any translational or rotational DoFs of the center nodes.

The local coordinate system of each connector element was chosen to be aligned with the screw axis. The direction of the screw axis was identified by finding the Eigenvector of the screw nodeset with the largest Eigenvalue. This vector was standardized to point in volar rather than dorsal direction and represented the local axis x' . The y' -axis was then defined to be in-plane with a vector parallel to the global y -axis and perpendicular to the local x' -axis. The z' -axis was obtained by computing the cross product of the x' - and y' -axis.

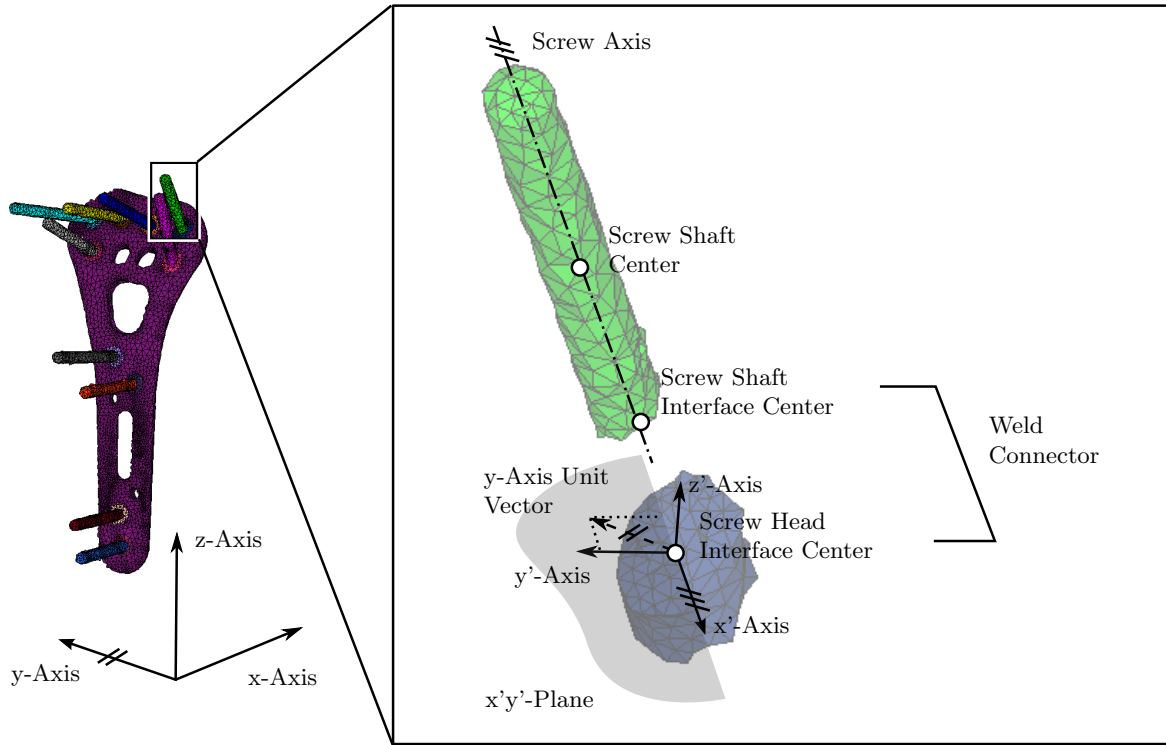


Figure 2.25: Screw-Plate interface connector and local orientation

2.2.7 FE model Solving and Postprocessing

A displacement of 0.6mm in negative z-direction was applied on the reference node of the model. This magnitude of displacement was chosen such that FE and experimental behaviour of the bone-implant system could be compared within the elastic range. Geometrical nonlinearity was enabled in Abaqus to account for large displacements and the material model of Schwiedrzik et al. [64] was included as a user defined material. Forces and displacements at the nodes, connector forces and moments, element stresses and strains as well as the damage variable were chosen as the output parameters.

The spring stiffnesses of the FE models were computed based on the forces and displacements of the reference node in z-direction. It was defined as the ratio of the force and displacement evaluated at the very first increment.

The connector forces and moments were also evaluated at the first increment. Forces along the screw axis, the amplitude of the shear forces in the perpendicular plane as well as the total moment were computed. Normal and shear forces were normalized by the reference node load in z-direction. The moments were normalized with the same force, acting at a lever arm of 10mm. This lever arm was chosen in approximation of the distance of the plate and loading axis.

2.3 Validation

The predictive capabilities of the model were quantified by computing the correlation of the experimental and FE spring stiffness. As the compliance of the experimental test-setup, e.g. from sensors, was not included in the FE model, it was estimated from compression tests without a specimen being mounted. Machine compliance tests and the statistics used for validation are presented in the following sections.

2.3.1 Machine Compliance

Ideally, the experimental test setup would exhibit infinite stiffness. Sensors and other materials in series with the tested specimen do, however, introduce a compliance into the system which was not modelled in the FEA. In order to account for this difference, the machine stiffness K_M was measured and the FE stiffness K_{FE} was corrected by adding a spring in series:

$$K_{FE,CORR} = \frac{1}{\frac{1}{K_M} + \frac{1}{K_{FE}}} \quad (2.16)$$

The machine stiffness was measured in the experimental setup by removing the specimen and the shells of both the proximal and distal container and applying 10 load cycles with an amplitude of 0.1mm at a rate of 1mm/s. The linear range of each cycle was selected manually and a linear regression was performed. The average of the slope of all cycles was defined as the machine stiffness.

2.3.2 Statistics

Experimental and FE spring stiffness were plotted against each other for all specimens. Linear regression analysis [55] was then performed to find the slope and intercept of the straight line relating the results. The goodness of the fit was quantified by computing R^2 and the standard error of the estimate (SEE). For comparisons of samples with different sizes, R^2 was adjusted for the sample size. The SEE serves as a measure of the deviation of the data points with respect to the fitted line. Both the FE and experimental stiffness were standardized by the sample mean to obtain a relative SEE, expressed in percent. An F-test was conducted to ensure that the model did not arise from random variations. The null hypothesis of this test was that the slope was zero.

A prerequisite for the validity the linear regression is the homoscedasticity and normality of the residuals. Homoscedasticity was assessed graphically in a plot of residuals against fitted values. A clear increase of the residual variance would indicate a violation of the homoscedasticity assumption. Ideally, the residuals are distributed in a symmetric band around zero and do not exhibit specific patterns. Residual normality was assessed in a probability plot and with a Shapiro-Wilk test. The probability plot displays the residuals on the y-axis and the theoretical quantiles of a normal distribution on the x-axis. In case the data points form a

straight line, it is very likely that the sample was drawn from a normally distributed population. Normality was also assessed quantitatively by conducting a Shapiro-Wilk test. The null hypothesis of this test is that the sample was drawn from a normal distribution. Rejection of the null hypothesis would, therefore, indicate that normality is highly unlikely.

Bland-Altman plots [71] were computed to visualize the validation results and to find systematic errors. In this plot, the difference of the FE and experimental spring stiffness of each sample were plotted against the mean of both values. The mean difference of all samples is displayed as a horizontal line to display systematic deviations. In order to assess the variance of the results, two horizontal bars indicate the mean plus/minus two times the residual standard deviation.

Additionally, descriptive statistics were conducted on both the experimental and FE datasets. A level of significance of 0.05 was chosen for all statistical tests. All statistical analysis were performed in Python using SciPy and the statsmodels module.

Chapter 3

Results

The results are structured in accordance to the Chapter 2 and present the results of the biomechanical experiments, FE analysis and the validation in individual sections.

3.1 Biomechanical Experiments

34 specimens were tested successfully in the biomechanical experiments. The mean donor age was 79.8 ± 12.8 years and 55.8% were male. Results of the yield force and stiffness computation and their correlation are presented in the subsequent sections. Additionally, a qualitative description of the failure modes observed in the experiments is provided in the final section.

3.1.1 Experimental Stiffness and Yield Force

Force-displacement curves of all specimens are shown in Figure 3.1. The elastic range was determined using the R^2 -method (see Section 2.1.3) and is indicated by the yield point (yellow dot). The dashed red line is the best fit within the elastic range and its slope represents the spring stiffness. Table 3.1 provides the minimum and maximum values, as well as mean and standard deviations (SD) of the computed stiffness and yield forces.

	Min	Max	Mean	SD
Stiffness [N/mm]	410.11	1235.00	755.21	186.81
Yield Force [N]	73.55	458.00	195.55	69.5

Table 3.1: Results of the biomechanical experiments

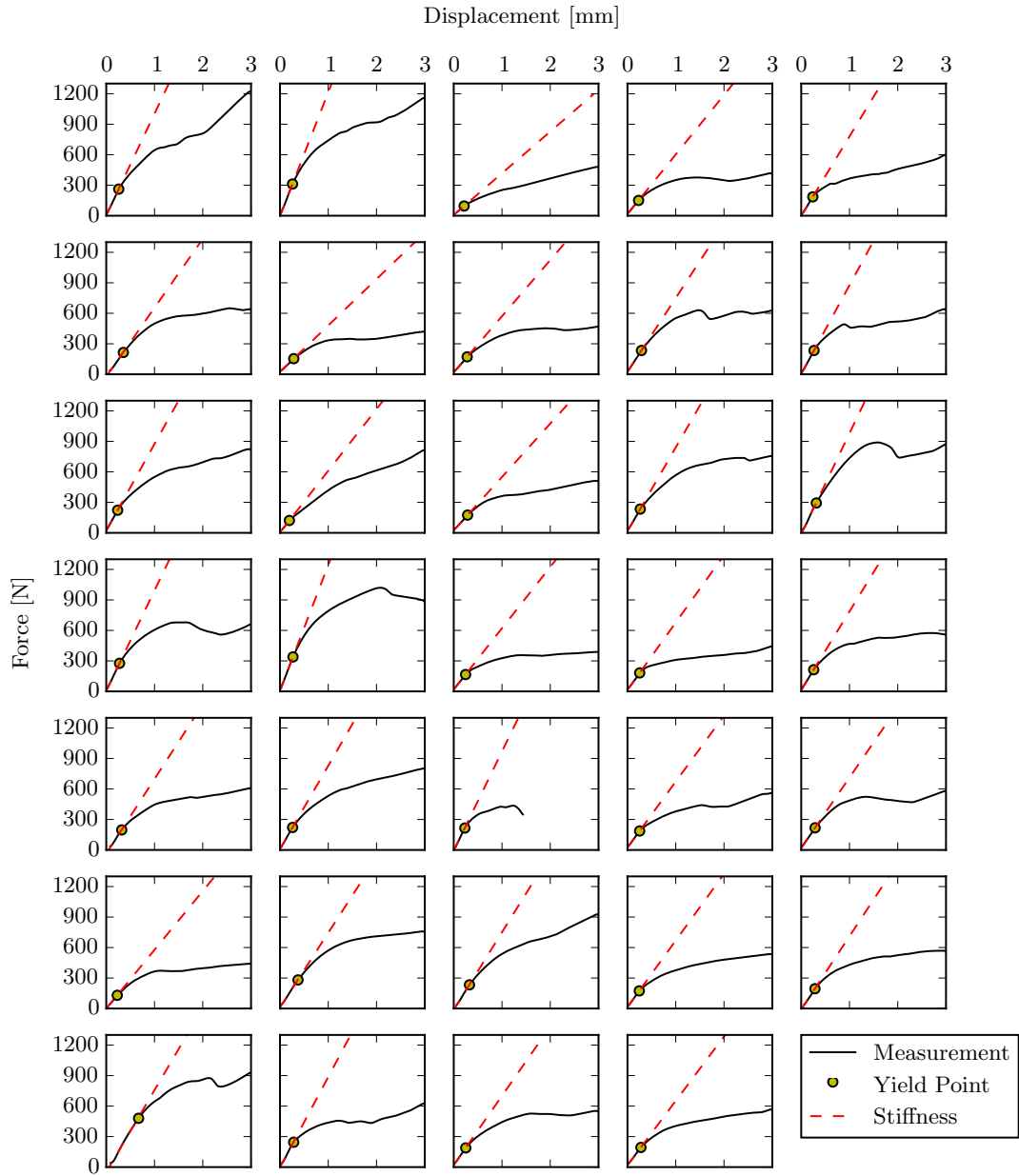


Figure 3.1: Cumulative plot of the 34 load-displacement curves

3.1.2 Correlation of Experimental Stiffness and Yield Force

Results of the linear regression are displayed in Figure 3.2 and Table 3.2. One outlier was excluded from the regression as it exceeded the 75% quartile plus 3 times the interquartile range and is indicated with a black cross symbol. Explanations for exclusion are provided in the discussion (see Section 4.1). The red line indicates the linear regression curve, with the 95% confidence intervals (CI) of the mean (black, dotted) and estimate (black, dashed).

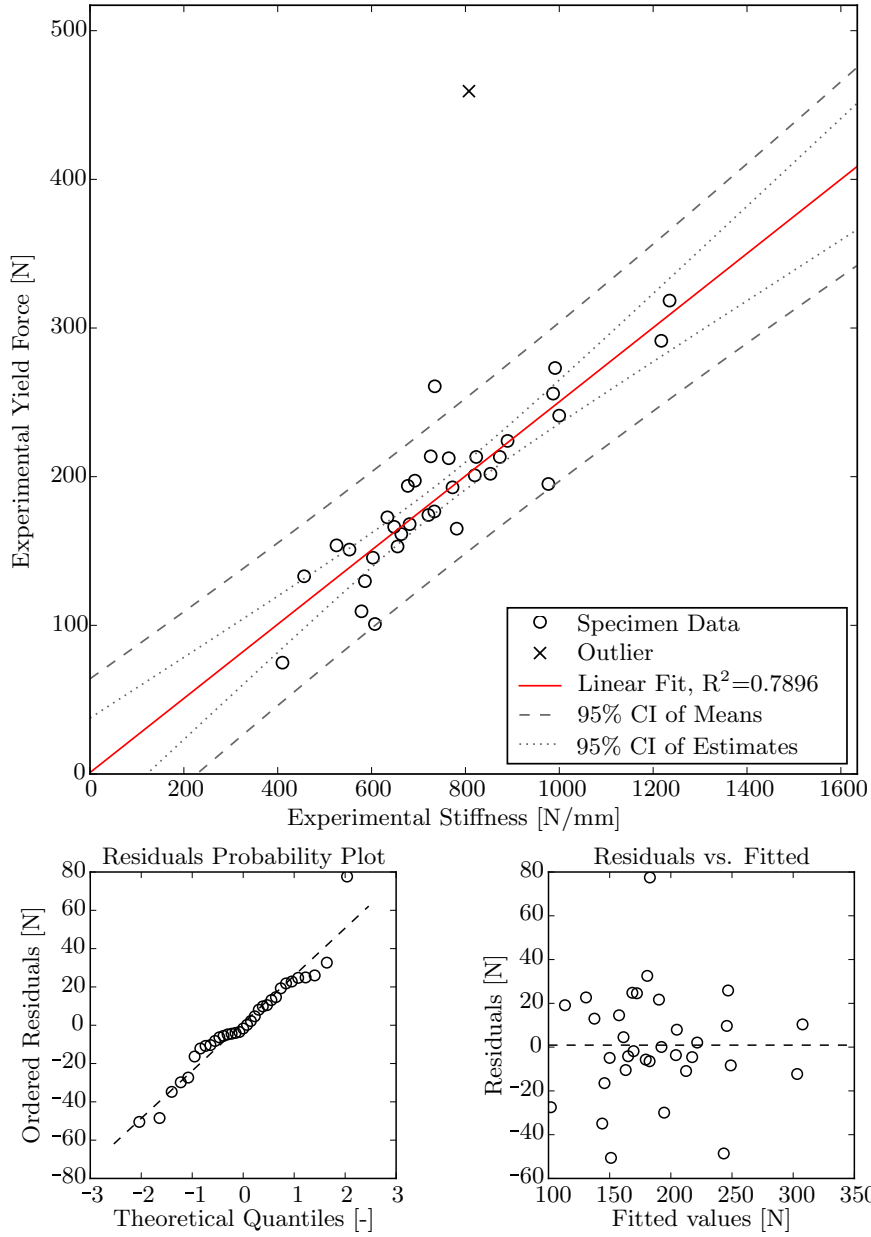


Figure 3.2: Linear regression of the experimental stiffness and yield force

Slope [mm]	Intercept [N]	R^2 [-]	SEE [%]	p-value [-]
0.2494	-0.3615	0.7896	13.4	<0.0001

Table 3.2: Results of the linear regression of the experimental stiffness and yield force

A significant correlation ($p < 0.0001$) was found with a goodness of fit of $R^2 = 0.7896$. Residuals were distributed approximately symmetrically around zero and the hypothesis of the normality could not be rejected with the Shapiro-Wilk test ($p = 0.135$).

3.1.3 Failure Mechanism

Visual inspection of the tested specimen revealed that failure occurred particularly at the screw-plate interface. This failure appeared as permanently tilted and even pushed out screws. An example of screw push-out is displayed on the left side of Figure 3.3. A total of 15 interface failures of this kind were observed in a total of 34 specimens. Figure 3.3 also shows a histogram of interface failures for all screws. Peaks were observed for failures at screws number 5 and 8 which failed 7 and 6 times, respectively.

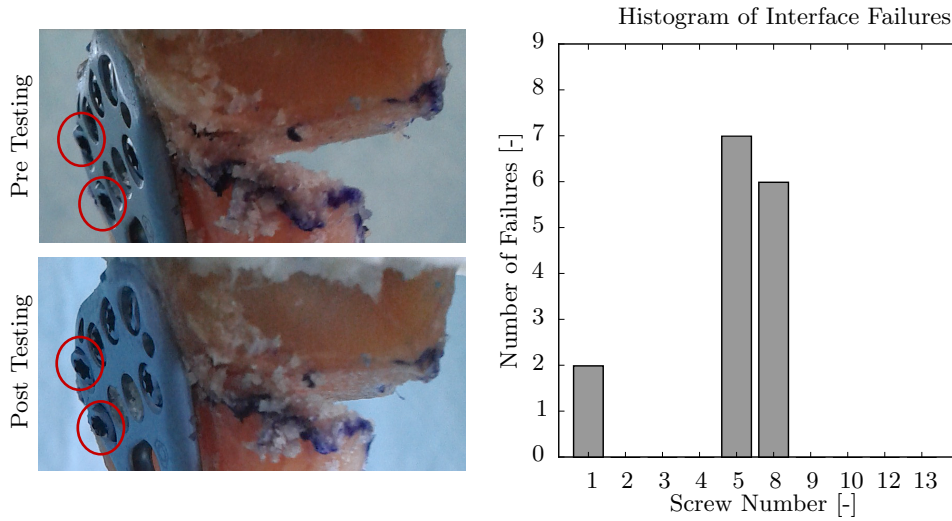


Figure 3.3: Exemplary screw-plate interface failure and histogram

3.2 Finite Element Analysis

All 34 specimens were modelled and analyzed. In the following sections, deformation, stress and damage plots of selected samples are presented. Section forces at the screw-plate interface are presented in the final section. The data was evaluated based on the full FE model which included the inhomogeneous, density and fabric based bone material.

3.2.1 Stiffness

Descriptive statistics of the spring stiffness are provided in Table 3.3. Minimum, maximum, mean and standard deviations are presented with and without correction for the machine compliance.

	Min	Max	Mean	SD
Stiffness [N/mm]	724.20	2319.83	1503.95	453.11
Corrected Stiffness [N/mm]	650.33	1700.96	1200.12	292.25

Table 3.3: Results of the FE analysis

The mean machine stiffness amounted to $6376.02 \pm 116.26 \text{ N/mm}$ and reduced the mean stiffness by approximately 300 N/mm .

3.2.2 Deformation

Deformation plots of specimens with low, average and high stiffness are displayed in Figure 3.4 at 0.6 mm displacement. Both a lateral and volar view are provided to judge the overall deformation of the bone-implant system.

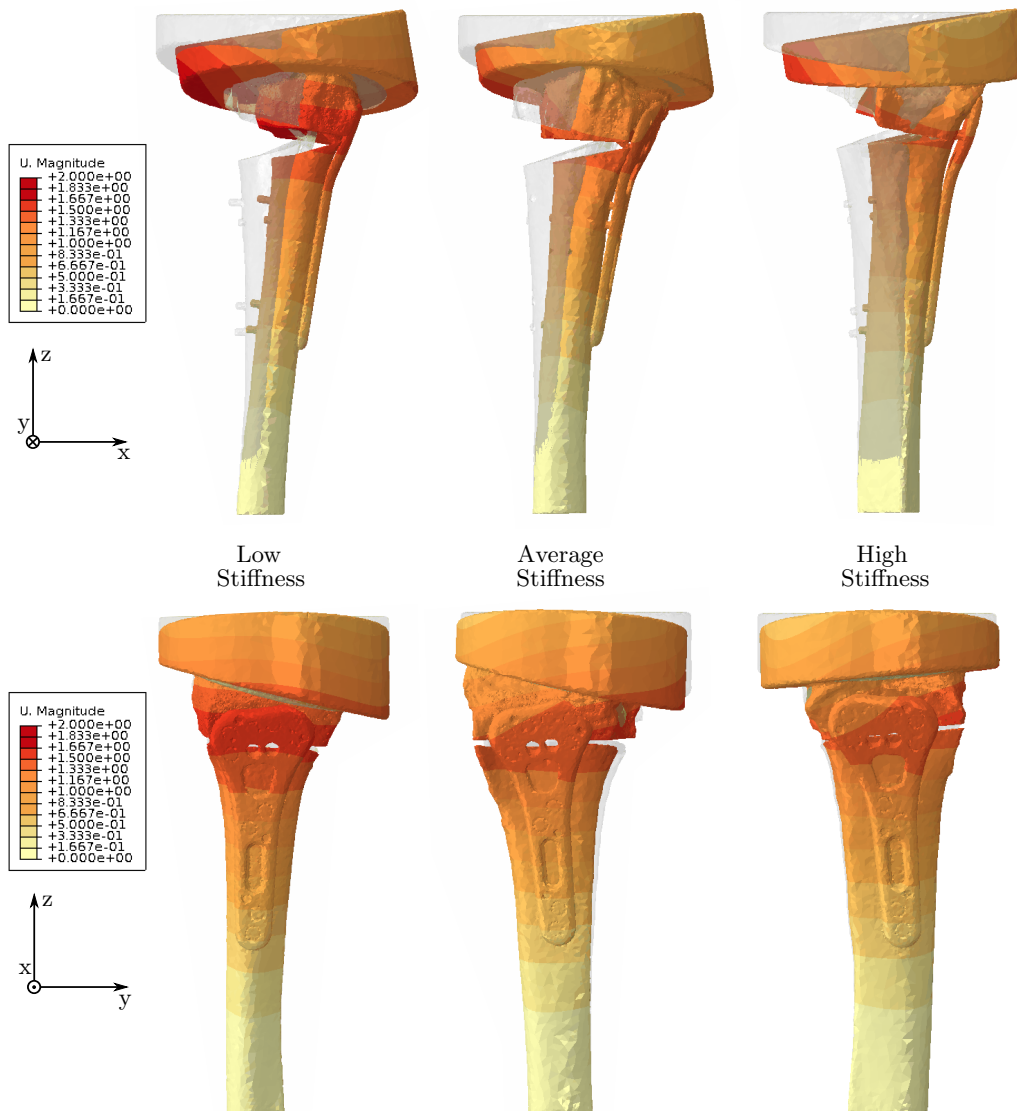


Figure 3.4: Deformation plots of three samples in volar and lateral view

The general motion pattern was similar for all specimen. Dorsal subsidence of the distal fragment lead to closure of the fracture gap and straightening of the implant. A minor tilt was observed around the dorso-volar axis (x-axis).

3.2.3 Stresses

Similarly to the deformations, stress plots are provided for low, average and high stiffness specimens at a displacement of 0.6mm. In Figure 3.5, von Mises stresses are plotted on the cortical bone and the implant. For the visualization, stresses were extrapolated to and averaged at the nodes.

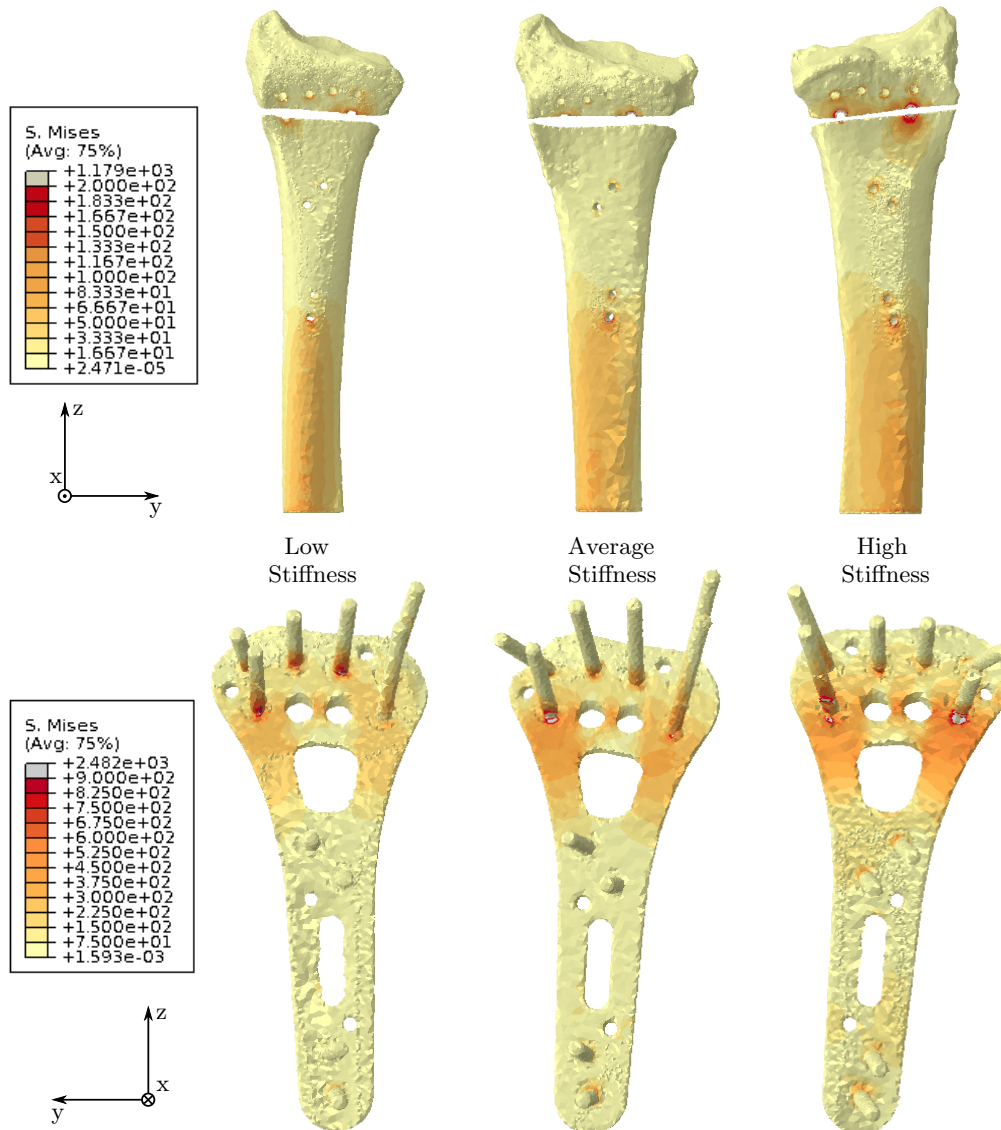


Figure 3.5: Bone and implant stress plots of three samples

Particularly high stresses were observed in the surrounding of screws number 5, 8 and 13 in the cortical bone. Stresses in the implant were generally pronounced at the screw-plate interface and at the height of the fracture gap. Screw-plate interface stresses were specifically large at screws number 5 and 8 in the specimens with average and high stiffness.

3.2.4 Damage

The bone damage variable is visualized in volar view and a coronal cut plane in Figure 3.6. Values larger than 1 and smaller than 0 might occur due to extrapolation and node averaging. The presented plots are, therefore, only interpreted qualitatively.

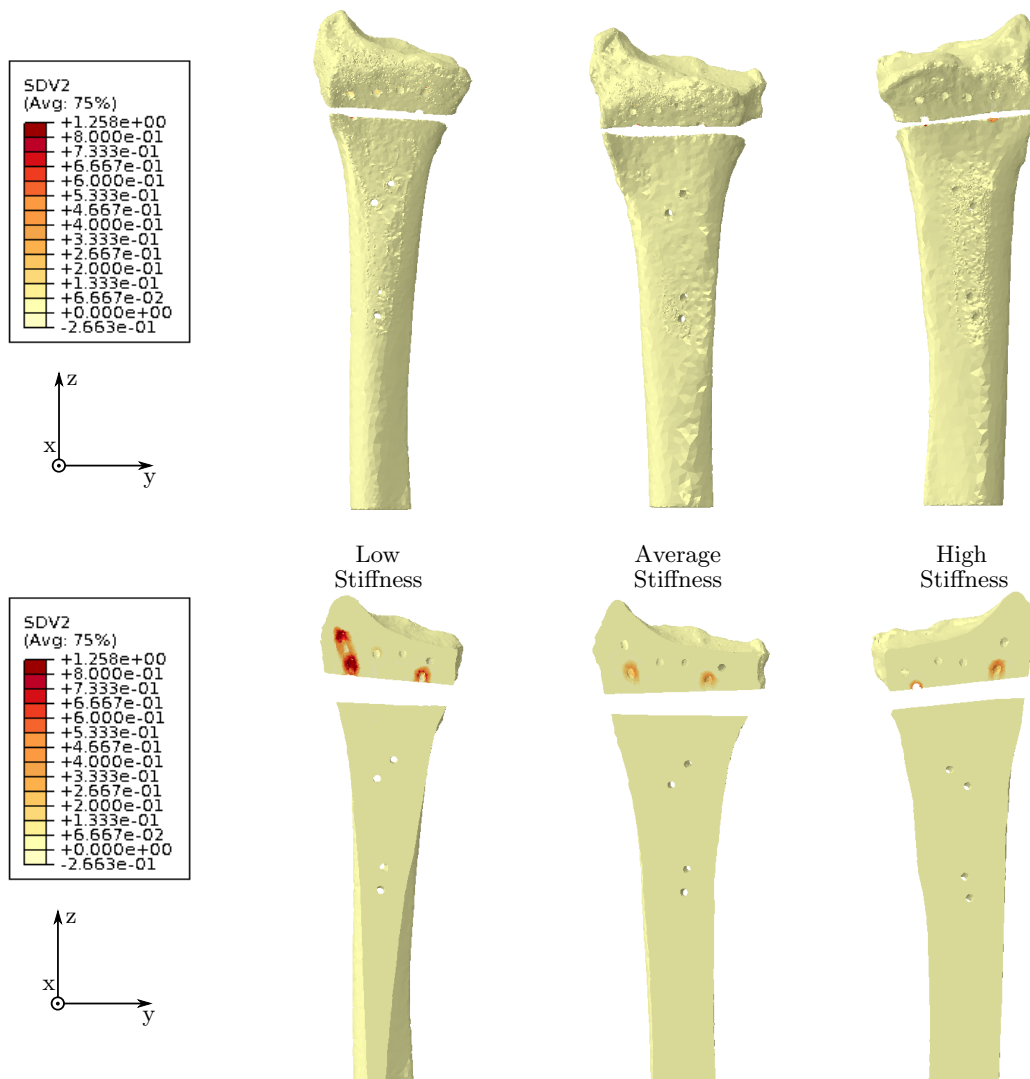


Figure 3.6: Exemplary plots of the damage variable

Only a small amount of damage was observed in the cortical bone. The trabecular bone exhibited pronounced damage around screws number 5 and 8 as well as number 1 in the sample with a low spring stiffness.

3.2.5 Screw-Plate Interface Forces

Figure 3.7 displays the section forces and moments computed for an individual sample and provides an example of the orientation of force and moment vectors. Distal screws predominantly transferred loads in normal direction, while large shear loads were found at the screw-plate interface of shaft screws. The moment vectors were majorly aligned with the latero-medial axis and larger for the distal screws.

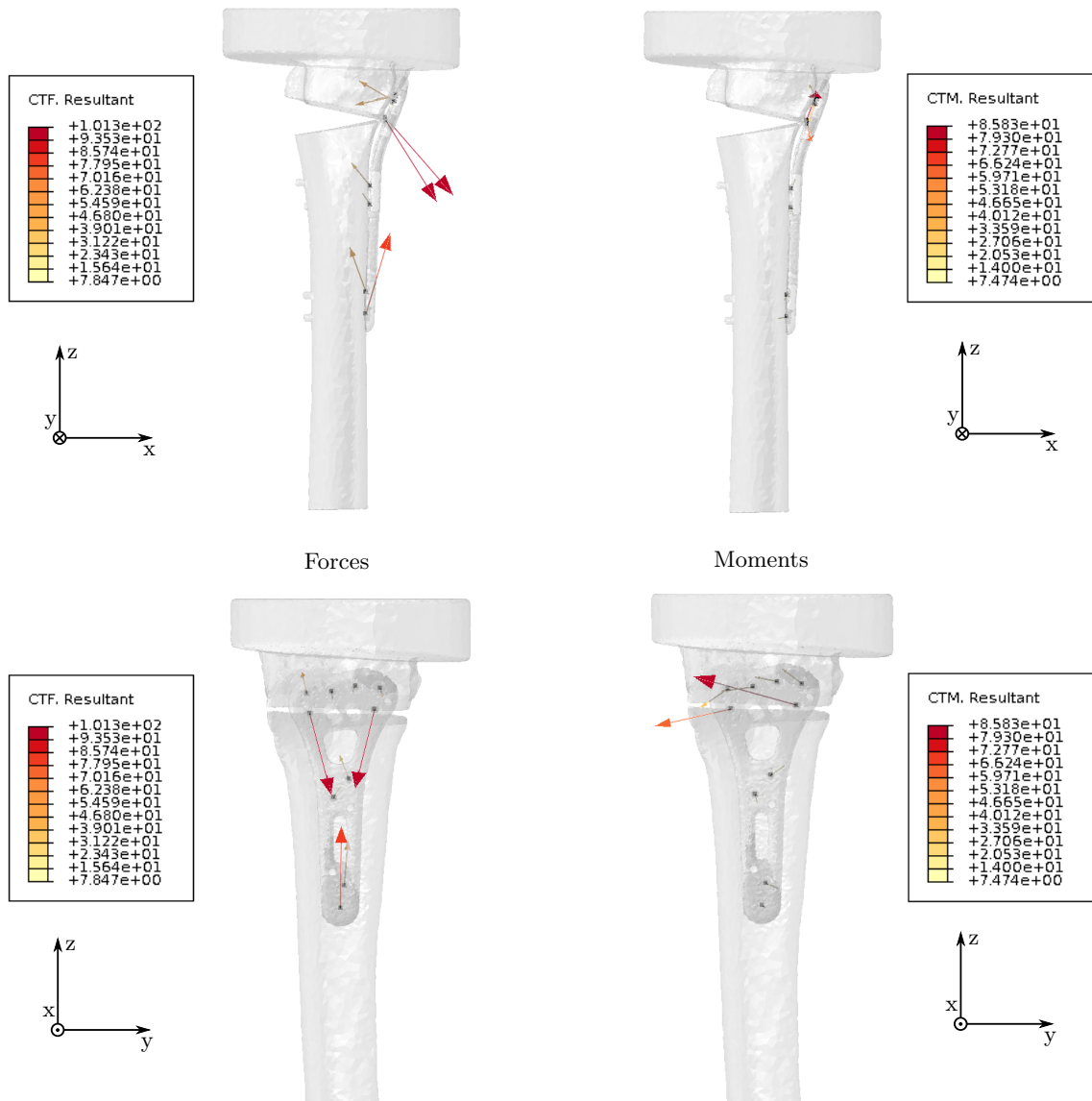


Figure 3.7: Orientations of force and moment vectors at the screw-plate interface of a single specimen

Figure 3.8 shows the relative screw loads for all screws of 34 specimen. The image gives an overview of the load distribution on the implant plate with circular markers, adapted in size to the mean magnitude of the normal force, shear force and moment. Standard deviations are indicated by the black circles and screws are labelled with their number as defined in Section 2.1.1. Blue and red colors indicate compressive and tensile forces at the interface, respectively.

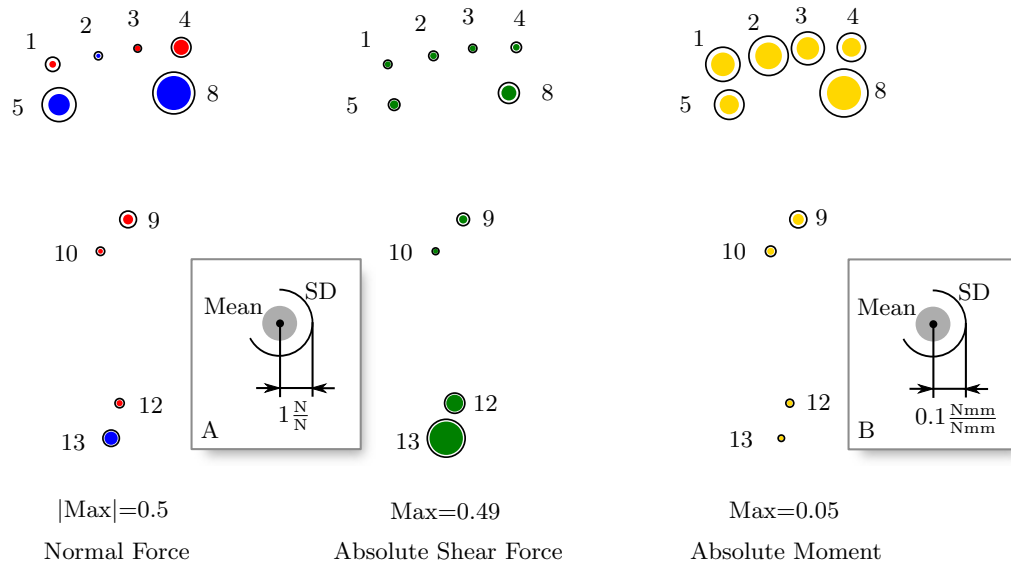


Figure 3.8: Averaged section forces and moments at the screw-plate interface. Scales for the forces and moments are provided in boxes (A) and (B), respectively.

Compressive normal forces were largest for screws number 5 and 8. Tensile forces were lower in magnitude due to a more homogeneous distribution in the most distal screw row. Variation in normal screw loads were most pronounced in screw number 5. In the shaft, only screw number 13 transferred compressive loads. Shear forces were most pronounced in screw number 13 which was exposed to approximately 50% of the total axial force on the specimen. Homogeneous distribution of shear loads was observed in the distal screws. Moments were largest at the interface to screw number 8 but approximately equally distributed among distal screws. A lower moment was observed for more proximal screws at the shaft.

3.3 Validation

The final validation results are presented in the subsequent section. Influences of the machine compliance, the used bone material model as well as screw types are added. One sample had to be excluded after identification as an extreme outlier (outside 3-times the interquartile range) in the residuals of the linear regression. Considerations about the reasons of exclusion are provided in the discussion section (see Section 4.3). As a result, only 33 specimen were considered in the validation.

3.3.1 Full Model Validation

In this section, the validation of the FE modelling approach using the orthotropic, density and fabric based bone material model and correction for machine compliance is presented. In Figure 3.9, the FE and experimental stiffnesses are plotted against each other to judge the correlation.

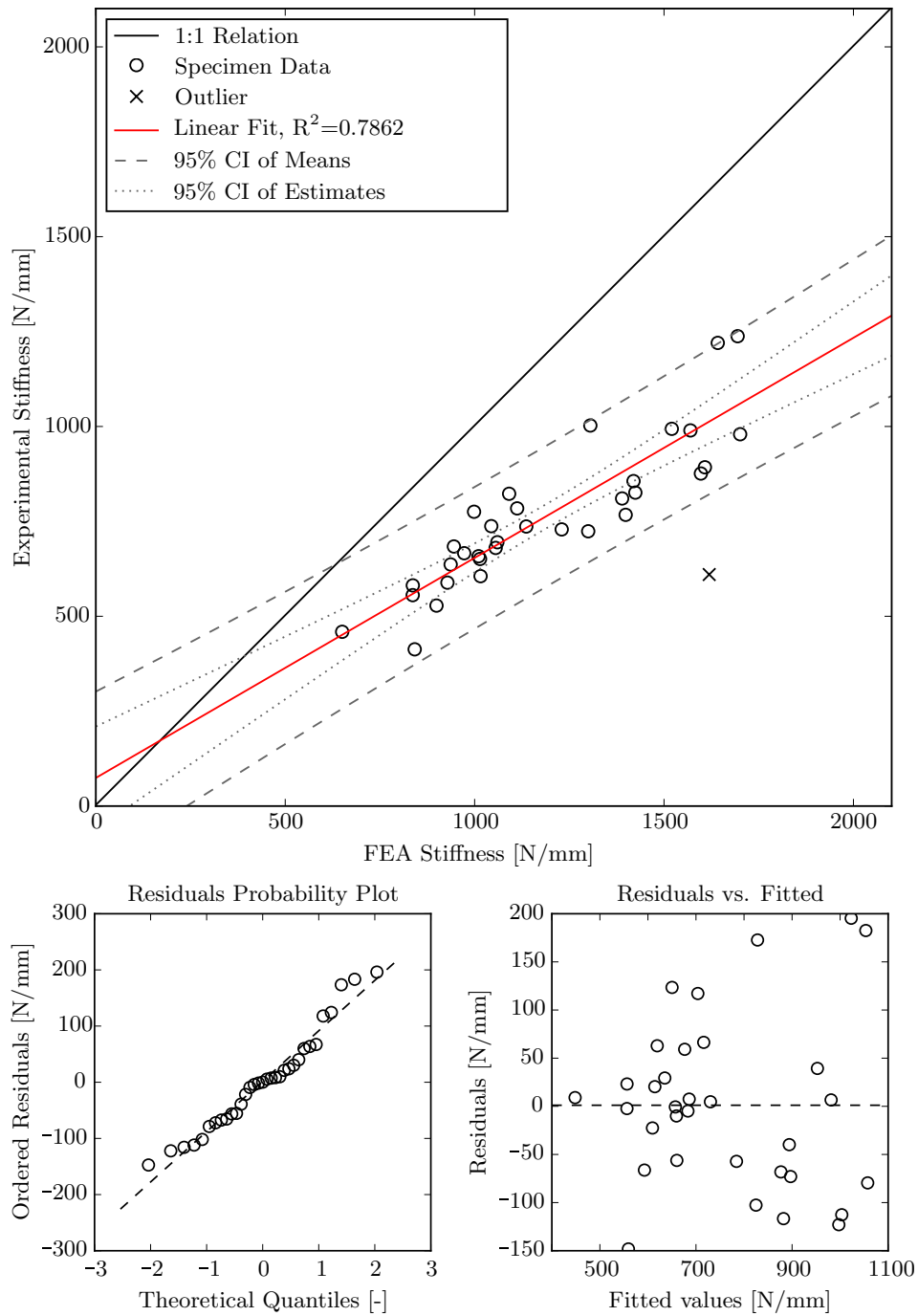


Figure 3.9: Linear regression of the full FE model

The outlier is indicated as a black cross and was excluded from the linear regression analysis. The red line indicates the linear regression curve, with the 95% confidence intervals (CI) of the mean (black, dotted) and estimate (black, dashed). The statistics of the linear regression are presented in Table 3.4. Despite the lack of a 1:1 relation, a high correlation with $R^2=0.7862$ was found. The F-test indicated that the slope was significantly different from zero ($p<0.0001$).

Slope [-]	Intercept [N/mm]	R^2 [-]	SEE [%]	p-value [-]
0.58	71.37	0.7862	11.8	<0.0001

Table 3.4: Results of the linear regression with the full FE model

The residual plots revealed a near symmetrical distribution of the residuals around zero and a slight increase of variation. Taking the small sample size into account, homoscedasticity was considered to be fulfilled nonetheless. The criterion of residual normality was satisfied both qualitatively as shown in Figure 3.9 as well as quantitatively ($p=0.214$).

The Bland-Altman plot is presented in Figure 3.10. The result is similar to the regression analysis: At low mean stiffnesses, FEA and experimental results are in good agreement as the difference is close to zero. Towards larger mean stiffnesses, the differences increase continuously. The positive sign indicates that FEA stiffnesses are larger over the whole stiffness range.

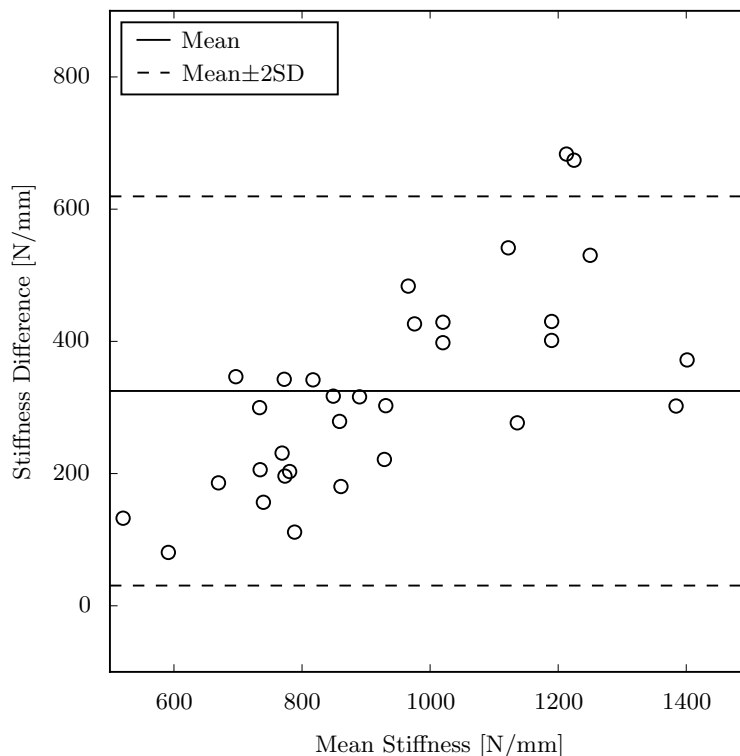


Figure 3.10: Bland Altman plot of FEA and experimental stiffness

3.3.2 Influence of the Machine Compliance

In this section, the influence of the machine compliance on the validation results is presented. Figure 3.11 shows the linear regression of the model with and without correction for the machine compliance. Corresponding statistics are provided in Table 3.5.

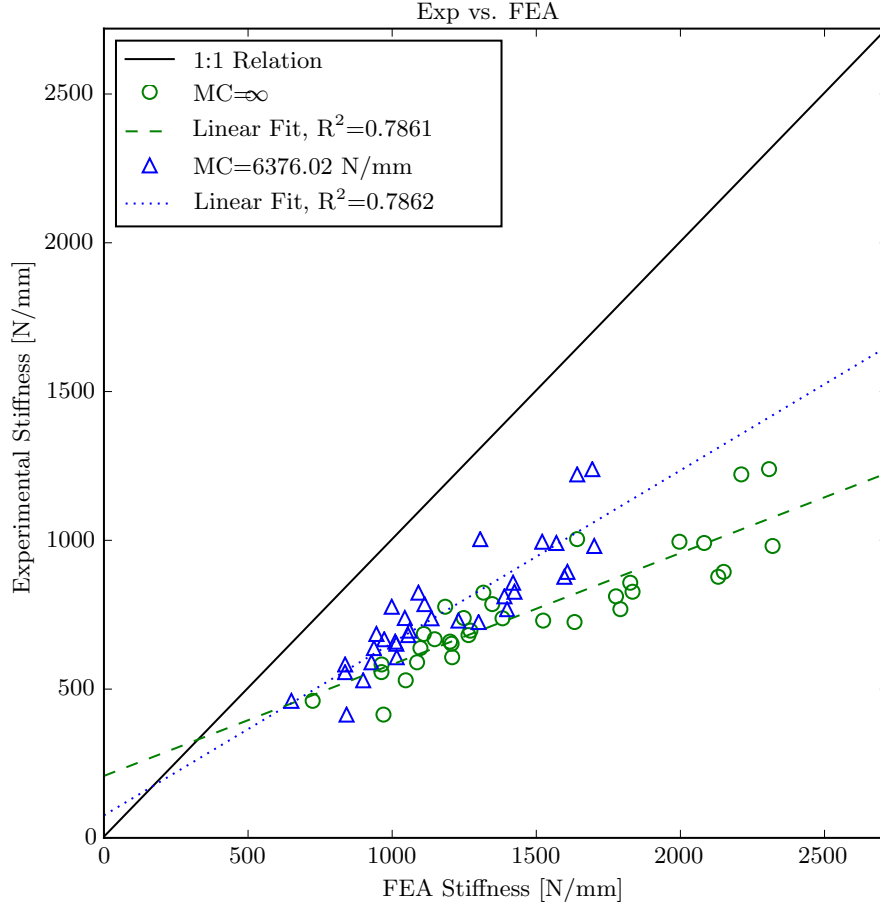


Figure 3.11: Validation with and without correction for machine compliance (MC)

MC [N/mm]	Slope [-]	Intercept [N/mm]	R^2 [-]	SEE [%]	p-value [-]
6376.02	0.58	71.37	0.7862	11.8	<0.0001
∞	0.37	204.00	0.7861	11.8	<0.0001

Table 3.5: Influence of the machine compliance (MC) on the linear regression

The machine compliance reduces the overall stiffness of the FE analysis and increases the slope of the regression line. Thus, including the machine compliance improved the prediction in terms of the aspired 1:1 relation. The goodness of the fit remained virtually unchanged.

3.3.3 Influence of the Bone Material Model

Differences between three approaches of bone material modelling are presented in this section, which will be denoted as Ortho-Inhom, Iso-Inhom and Iso-Hom (see Table 3.6 and Section 2.2.6).

Abbreviation	Cortex	Spongiosa
Iso-Hom	Isotropic, homogeneous	Isotropic, homogeneous
Iso-Inhom	Isotropic, density dependent	Isotropic, density dependent
Ortho-Inhom	Isotropic, density dependent	Orthotropic, density and fabric dependent

Table 3.6: Overview of the bone material symmetries and homogeneity

Figure 3.12 and Table 3.7 show a comparison of the validation results achieved with Ortho-Inhom, Iso-Inhom and Iso-Hom bone material. The spring stiffness of all models was corrected by the machine compliance.

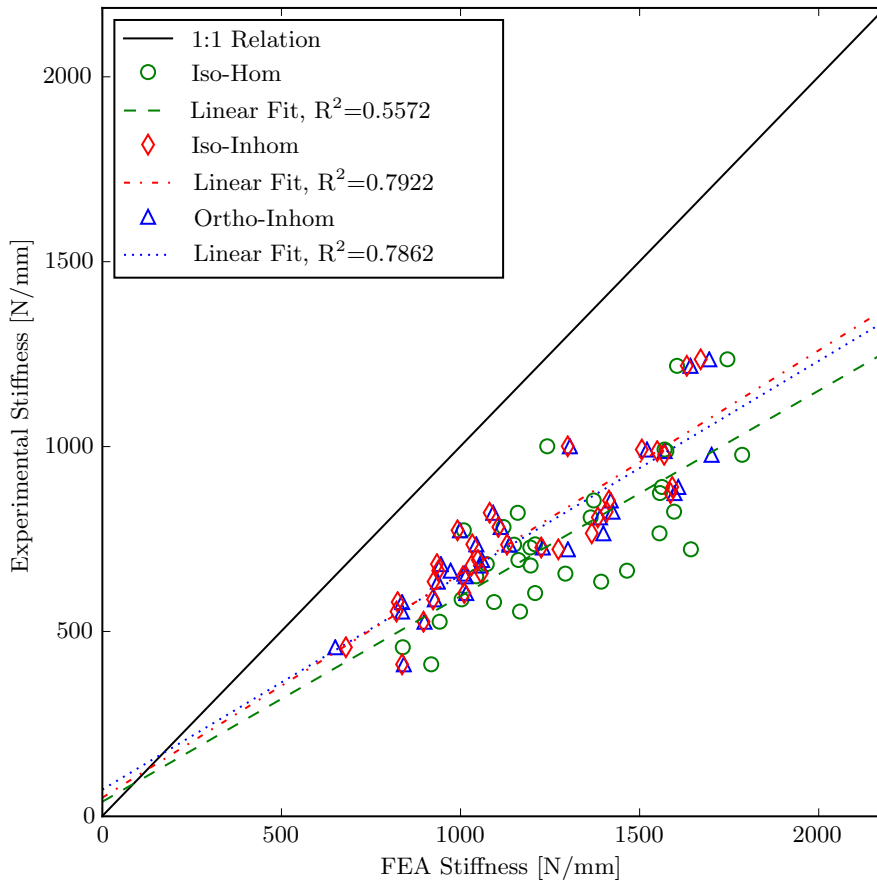


Figure 3.12: Validation with simple and complex bone material models

Model	Slope [-]	Intercept [N/mm]	R^2 [-]	SEE [%]	p-value [-]
Iso-Hom	0.56	38.60	0.5572	17.0	<0.0001
Iso-Inhom	0.60	49.48	0.7922	11.6	<0.0001
Ortho-Inhom	0.58	71.37	0.7862	11.8	<0.0001

Table 3.7: Influence of the bone material model on the linear regression

The isotropic homogeneous bone material model showed a considerably lower goodness of the fit an increased standard error. The slope of the regression line was similar in inhomogeneous and homogeneous models but the intercept was slightly lower in the latter. Using the ortho-topic and isotropic inhomogeneous models revealed only minor differences in slope, intercept and goodness of the fit.

3.3.4 Influence of the Screw Types

Two types of screws were used in the experiments: Standard and speedtip locking screws. The influence on the screw types on the validation is presented in this section. Figure 3.13 and Table 3.8 show a comparison of the validation of the whole dataset as well as subsets containing only standard and speedtip screws. Due to varying sample sizes, the adjusted goodness of the fit R_{adj}^2 is provided.

Screwtype	Slope [-]	Intercept [N/mm]	R^2 [-]	n [-]	R_{adj}^2 [-]	SEE [%]	p-value [-]
All	0.58	71.37	0.7862	33	0.7793	11.8	<0.0001
Speedtip	0.84	-232.03	0.8564	8	0.8326	12.9	<0.001
Standard	0.47	187.36	0.8135	25	0.8054	8.9	<0.0001

Table 3.8: Influence of the screw type on the linear regression

Separating the dataset into only standard and speedtip subsets improved the goodness of the fit R_{adj}^2 . The slope found for the speedtip subset was closer to 1 than for both the whole dataset and the standard screw subset but also exhibited an increased standard error.

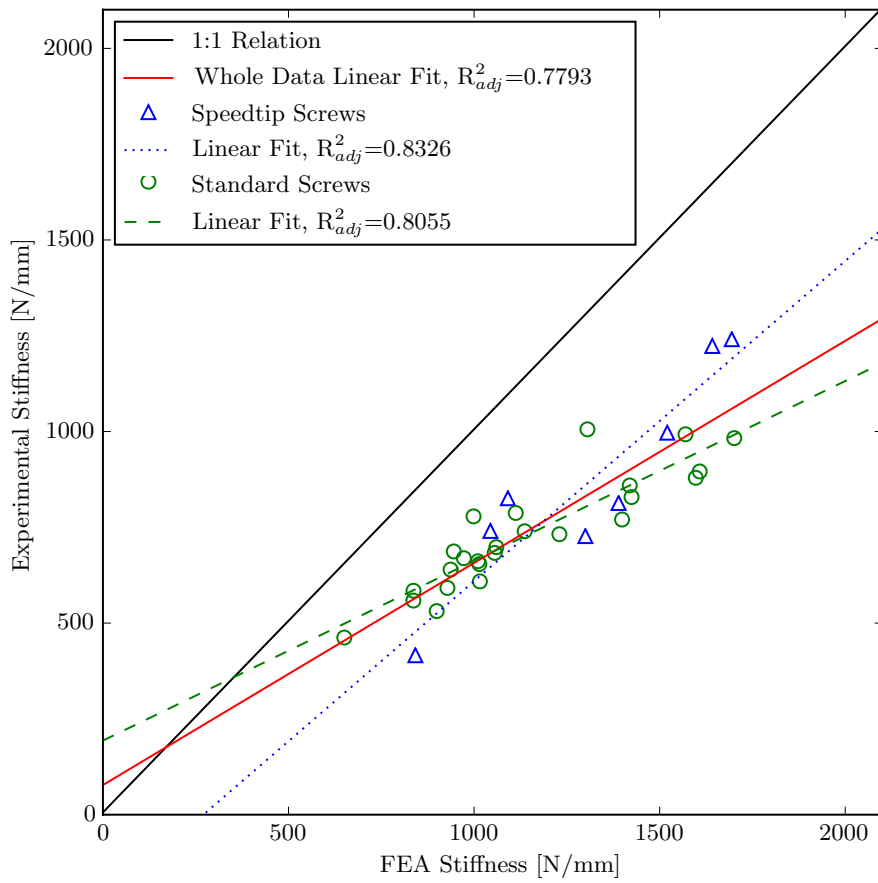


Figure 3.13: Validation with separated screw types

Chapter 4

Discussion

Biomechanical testing and specimen specific FE model generation was successfully conducted on 34 radii with extraarticular fractures and volar plate osteosynthesis. Spring stiffness validation was performed on 33 specimen as 1 specimen was identified as an outlier. Experimental and FE stiffness were highly correlated ($R^2=0.7862$, $p<0.0001$), indicating a strong correspondence of the real and simulated elastic response of the bone-implant system.

4.1 Biomechanical Experiments

A total of 34 specimen were tested in uniaxial compression tests. The measured load-displacement curves revealed a highly nonlinear behavior of the bone-implant system. All curves do, however, exhibit an initial linear region which was automatically identified by the custom Python scripts. The automatic evaluation of the stiffness and yield force diminished user errors but also had inherent limitations. In particular, the outlier mentioned in Section 3.1.2 exhibited an extended initial toe region possibly leading to overestimation of the yield point and underestimation of the stiffness.

The stiffness data gathered in the experiments are in good agreement with literature. The mean stiffness of 755.21N/mm found in this studies lies well within the range of 450 to 800N/mm as reported in biomechanical experiments of DRFs with volar plate osteosynthesis and similar test-setups [35, 15, 54]. Comparison of the yield force is hardly possible due to either unknown or different definitions of the yield point. McCall et al. [72] and Osada et al. [73] reported yield forces higher than observed in the present experiments, ranging from 360 to 1892 N. However, McCall et al. performed experiments on synthetic instead of cadaveric radii and computed the yield forces based on the 0.2% strain offset criterion without providing further information on the specimen reference length. Osada et al. used cadaveric but embalmed specimens and did not provide an exact definition of the yield point.

A regression analysis of the stiffness and yield force revealed a significant correlation ($R^2=0.79$, $p<0.0001$) in the presented experiment. Similar relations have already been found for failure loads and stiffnesses in intact radii [48], with a coefficient of determination of 0.75. As a result, the stiffness of the bone-implant system can be used not only to predict the fracture gap displacement at a given load, but also to estimate the failure onset.

The actual failure mechanism of the bone-implant system could be judged only based on pictures of the specimen before and after testing in the experiments. Visible damage or plastic deformation could be observed neither on the bone, nor on the implant plate. Excessively tilted and pushed-out screws, could, however, be identified in numerous tested samples. The screw-plate interface can therefore be considered as, at least, one of the weakest links of the bone-implant system.

4.2 FE Analysis

Specimen specific FE models were generated semi-automatically for 34 samples. After the work flow and the Blender template file were established, manual intervention was necessary only for positioning the implant, embedding and fracture gap as well as pre-positioning the HR-pQCT surface for registration. All these steps could be conducted in Blender with a custom made user-interface which further decreased the modelling effort.

The main cause of complexity in the presented model generation methodology was the necessity for validation. Conducting parameter studies would simplify the approach to manually or even automatically changing variables such as the implant position or screw orientations in the Blender file. Remaining steps to predict the bone-implant system are fully automatized in the work flow.

The mean spring stiffness of 1503.95N/mm found for the FE models lies above the range of values reported in literature. Lin et al. [49] computed the stiffness of FE models with isotropic, homogeneous, separated cortical and trabecular bone and volar plate osteosynthesis and found values of approximately 150N/mm. The most probable explanation of this deviation are the applied boundary conditions. In contrast to the model presented in this study, Lin et al. applied forces directly to the distal articular surface such that movements in the transversal plane were unconstrained. Mair et al. [52] reported a stiffness of approximately 600N/mm of a DRF treated with volar plate osteosynthesis. Mair et al. did, however, only model a single radius and both the bone material model and boundary conditions were not described adequately.

Besides spring stiffness, the deformation, stress, bone damage and the screw-plate interface forces were evaluated in the generated FE models. These variables allow a deeper insight into the mechanisms of the bone-implant system. Deformation plots revealed a plausible motion of the distal fragment and bending of the implant plate. As expected, stresses in the bone are concentrated in the near surrounding of the screws and particularly expressed at the screw-bone interface of screws number 5, 8 and 13. This finding is consistent with the evaluated screw-plate interface forces. Similarly, bone material damage was observed around screws number 5 and 8.

Rather than just comparing the apparent stiffness or yield point as obtained in the biomechanical experiments, the FE results allow a more profound judgement of the implant system. In particular, the results revealed the inhomogeneous load distribution in the two distal screw rows. Screws number 5 and 8 were exposed to excessive normal forces, leading to a likely failure at the screw-plate or screw-bone interface.

4.3 Validation

The validation of the simulated spring stiffness was conducted in 33 specimen. One outlier was eliminated from the regression analysis. A possible explanation was found after visual comparison of the real and FE modelled specimen: Barely any contact was observed between screw number 5 and the distal fragment in the real specimen. In the modelled specimen, however, the screw was in contact with the distal fragment. The fully bonded contact conditions and the high loads transferred at this screw might then have lead to the excessive deviation between experimental and simulated results.

In general, the linear regression analysis showed a significant correlation ($R^2=0.7862$, $p<0.0001$) with a low relative standard error of the estimate (11.3%). A 1:1 relation between experimental and simulated values was not obtained. Instead, the slope of 0.37 indicated considerable overestimation of the experimental stiffness. Including the machine compliance improved the slope to 0.58 but could not explain the deviations to the full extent. Numerous reasons might explain the remaining systematic error. First, the machine compliance might have been larger than measured. Second, cutting 40mm of the proximal bone and neglecting the proximal embedding might have increased the stiffness. Third, the used material constants might overestimate the bone stiffness for the radius as they were obtained by averaging over bones of different anatomical sites [65]. Fourth, the screw-bone interface stiffness modelling might be incorrect. Using fully bonded contact in FE models was already reported to overestimate the apparent stiffness [74]. Finally, also the fully bonded conditions at the screw-plate interface might vary from the actual interface compliance. However, no study is known to the author which addresses this issue.

The comparison of validation results with different bone material models showed that including the local bone volume fraction is essential to decrease the error of the prediction. Material orthotropy could, however, not improve the prediction substantially. As a result, FE models which assume trabecular and cortical bone phases as homogeneous materials run into higher risk of wrong stiffness predictions.

Differences were also found when validating the groups of specimens prepared with speedtip and standard locking screws separately. A higher coefficient of determination and a lower relative standard error of the estimate were found for the individual groups compared to the group containing all screw types. Also, the slope was considerably higher in the speedtip group. It could be hypothesized that the fully bonded conditions at the bone-screw interface of the FE models more closely resemble the fixation with speedtip screws. A plausible explanation is the skipped step of pre-drilling during preparation with the speedtip screws, leading to a tighter contact with the bone.

The validity of the section forces evaluated at the screw-plate interface could be assessed qualitatively by comparison with the experimental failure mechanism. Experimental screw-plate interface failure was observed particularly at screws number 5 and 8. This was consistent with the screws transferring the highest compressive loads to the implant plate in the FE model. Screw number 5 might be more likely to fail as it was inserted at a steeper angle with respect to the implant plate than screw number 8.

4.4 Limitations

Several limitations of this validation study need to be discussed. First of all it has to be mentioned that the FE model aimed at resembling the ex-vivo biomechanical experiment rather than the in-vivo situation. The ex-vivo experiment itself contains obvious limitations such as neglecting soft tissue and ulnar bone as well as possibly unphysiological loading conditions. Second, the FE model included only crude approximations of the screw-bone, screw-plate and plate-bone interfaces. More complex interface conditions could, however, not be incorporated due to the lack of experimental data. Finally, the FE model was validated in one load case only. Conducting tests with different loading directions or boundary conditions would improve the validation but was not feasible in the experimental studies.

4.5 Conclusion

A significant correlation was found between the spring stiffness computed in biomechanical experiments and FE models of extra-articular DRFs with volar plate osteosynthesis. As experimental stiffness and yield force were found to be correlated, the predicted stiffness values also contains information on the failure onset of the bone-implant system. The FE model stiffness was larger than the experimental stiffness in all samples. Fully bonded screw-bone and screw-plate interfaces might cause this deviation and require further investigations. In any case, utilizing homogeneous instead of inhomogeneous trabecular and cortical bone material leads to a substantial decrease of the goodness of the linear regression.

Bibliography

- [1] Koo, K. O. T., Tan, D. M. K., and Chong, A. K. S. (2013) Distal radius fractures: an epidemiological review. *Orthopaedic surgery*, **5**, 209–13.
- [2] Handoll, H. H. G. and Madhok, R. (2002) Managing fractures of the distal radius in adults. Clinical and research implications from systematic reviews of existing trials. *Acta orthopaedica Scandinavica. Supplementum*, **73**, 45–8.
- [3] Marieb, E. N. and Hoehn, K. N. (2013) *Human anatomy & physiology*. Pearson, 9th edn.
- [4] Wang, X., Nyman, J., and Dong, X. (2010) Fundamental biomechanics in bone tissue engineering. *Synthesis Lectures on Tissue Engineering*, **2**, 1—225.
- [5] Kotwal, P. P.; Garg, B. (2008) Fractures of the distal radius: Current Concepts. *Journal of Orthopaedics*, **10**, 34–41.
- [6] Schmitt, R. (2008) *Bildgebende Diagnostik der Hand: 362 Tabellen*. Georg Thieme Verlag.
- [7] Hamill, J. and Knutzen, K. M. (2008) *Biomechanical Basis of Human Movement*. Lippincott Williams & Wilkins, third edn.
- [8] AO Foundation (2007), Distal radius - Diagnosis. www.aofoundation.org.
- [9] Müller, M. E., Koch, P., Nazarian, S., and Schatzker, J. (1990) *The Comprehensive Classification of Fractures of Long Bones*. Springer Berlin Heidelberg.
- [10] Simic, P. M. and Weiland, A. J. (2003) Fractures of the Distal Aspect of the Radius: Changes in Treatment Over the Past Two Decades. *The Journal of Bone & Joint Surgery*, **85**, 552–564.
- [11] AO Foundation (2007), Distal radius - Reduction and Fixation. www.aofoundation.org.
- [12] Obert, L., Rey, P.-B., Uhring, J., Gasse, N., Rochet, S., Lepage, D., Serre, A., and Garbuio, P. (2013) Fixation of distal radius fractures in adults: a review. *Orthopaedics & traumatology, surgery & research : OTSR*, **99**, 216–34.
- [13] Crosby, S. N., Fletcher, N. D., Yap, E. R., and Lee, D. H. (2013) The mechanical stability of extra-articular distal radius fractures with respect to the number of screws securing the distal fragment. *The Journal of hand surgery*, **38**, 1097–105.

- [14] Drobetz, H., Weninger, P., Grant, C., Heal, C., Muller, R., Schuetz, M., Pham, M., and Steck, R. (2013) More is not necessarily better. A biomechanical study on distal screw numbers in volar locking distal radius plates. *Injury*, **44**, 535–9.
- [15] Trease, C., McIlff, T., and Toby, E. B. (2005) Locking versus nonlocking T-plates for dorsal and volar fixation of dorsally comminuted distal radius fractures: a biomechanical study. *The Journal of hand surgery*, **30**, 756–63.
- [16] Hart, A., Collins, M., Chhatwal, D., Steffen, T., Harvey, E. J., and Martineau, P. A. (2014) Can the Use of Variable-Angle Volar Locking Plates Compensate for Suboptimal Plate Positioning in Unstable Distal Radius Fractures? A Biomechanical Study. *Journal of orthopaedic trauma*.
- [17] Rausch, S., Klos, K., Stephan, H., Hoffmeier, K., Gras, F., Windolf, M., Gueorguiev, B., Hofmann, G. O., and Mückley, T. (2011) Evaluation of a polyaxial angle-stable volar plate in a distal radius C-fracture model—a biomechanical study. *Injury*, **42**, 1248–52.
- [18] Schneppendahl, J., Windolf, J., and Kaufmann, R. A. (2012) Distal radius fractures: current concepts. *The Journal of hand surgery*, **37**, 1718–25.
- [19] Mehling, I., Müller, L. P., Delinsky, K., Mehler, D., Burkhart, K. J., and Rommens, P. M. (2010) Number and Locations of Screw Fixation for Volar Fixed-Angle Plating of Distal Radius Fractures: Biomechanical Study. *The Journal of Hand Surgery*, **35**, 885–891.
- [20] Costa, M. L., Achten, J., Parsons, N. R., Rangan, A., Griffin, D., Tubeuf, S., and Lamb, S. E. (2014) Percutaneous fixation with Kirschner wires versus volar locking plate fixation in adults with dorsally displaced fracture of distal radius: randomised controlled trial. *BMJ (Clinical research ed.)*, **349**, g4807.
- [21] Appel, L. J. (2006) A primer on the design, conduct, and interpretation of clinical trials. *Clinical journal of the American Society of Nephrology : CJASN*, **1**, 1360–7.
- [22] Grewal, R., MacDermid, J. C., King, G. J. W., and Faber, K. J. (2011) Open reduction internal fixation versus percutaneous pinning with external fixation of distal radius fractures: a prospective, randomized clinical trial. *The Journal of hand surgery*, **36**, 1899–906.
- [23] Kawasaki, K., Nemoto, T., Inagaki, K., Tomita, K., and Ueno, Y. (2014) Variable-angle locking plate with or without double-tiered subchondral support procedure in the treatment of intra-articular distal radius fracture. *Journal of orthopaedics and traumatology: official journal of the Italian Society of Orthopaedics and Traumatology*.
- [24] Aita, M. A., Vieira Ferreira, C. H., Schneider Ibanez, D., Saraiva Marquez, R., Hideki Ikeuti, D., Toledo Mota, R., Credidio, M. V., and Noboru Fujiki, E. (2014) Randomized clinical trial on percutaneous minimally invasive osteosynthesis of fractures of the distal extremity of the radius. *Revista Brasileira de Ortopedia (English Edition)*, **49**, 218–226.
- [25] Couzens, G. B., Peters, S. E., Cutbush, K., Hope, B., Taylor, F., James, C. D., Rankin, C. R., and Ross, M. (2014) Stainless steel versus titanium volar multi-axial locking plates for fixation of distal radius fractures: a randomised clinical trial. *BMC musculoskeletal disorders*, **15**, 74.

- [26] Grindel, S. I., Wang, M., Gerlach, M., Mcgrady, L. M., and Brown, S. (2007) Biomechanical Comparison of Fixed-Angle Volar Plate Plus Fragment-Specific Fixation in a Cadaveric Cadaveric Distal Radius Fracture Model. *The Journal of hand surgery*, **32**, 194–199.
- [27] Kamei, S., Osada, D., Tamai, K., Kato, N., Takai, M., Kameda, M., and Nohara, Y. (2010) Stability of volar locking plate systems for AO type C3 fractures of the distal radius: biomechanical study in a cadaveric model. *Journal of orthopaedic science : official journal of the Japanese Orthopaedic Association*, **15**, 357–64.
- [28] Kandemir, U., Matityahu, A., Desai, R., and Puttllitz, C. (2008) Does a volar locking plate provide equivalent stability as a dorsal nonlocking plate in a dorsally comminuted distal radius fracture?: a biomechanical study. *Journal of orthopaedic trauma*, **22**, 605–10.
- [29] Kainz, H., Dall’Ara, E., Antoni, A., and Redl, H. (2013) Calcium phosphate cement augmentation after volar locking plating of distal radius fracture significantly increases stability. *European Journal of Orthopaedic Surgery and Traumatology*, **24**, 869–75.
- [30] Mehling, I., Klitscher, D., Mehling, A., Nowak, T., Sternstein, W., Rommens, P., and Müller, L. (2012) Volar fixed-angle plating of distal radius fractures: screws versus pegs—a biomechanical study in a cadaveric model. *Journal of orthopaedic trauma*, **26**, 395–401.
- [31] Rausch, S., Schlonski, O., Klos, K., Gras, F., Gueorguiev, B., Hofmann, G. O., and Mückley, T. (2013) Volar versus dorsal latest-generation variable-angle locking plates for the fixation of AO type 23C 2.1 distal radius fractures: a biomechanical study in cadavers. *Injury*, **44**, 523–6.
- [32] Dahl, W. J., Nassab, P. F., Burgess, K. M., Postak, P. D., Evans, P. J., Seitz, W. H., Greenwald, A. S., and Lawton, J. N. (2012) Biomechanical properties of fixed-angle volar distal radius plates under dynamic loading. *The Journal of hand surgery*, **37**, 1381–7.
- [33] Liporace, F. A., Kubiak, E. N., Jeong, G. K., Iesaka, K., Egol, K. a., and Koval, K. J. (2006) A biomechanical comparison of two volar locked plates in a dorsally unstable distal radius fracture model. *The Journal of trauma*, **61**, 668–72.
- [34] Wall, L. B., Brodt, M. D., Silva, M. J., Boyer, M. I., and Calfee, R. P. (2012) The effects of screw length on stability of simulated osteoporotic distal radius fractures fixed with volar locking plates. *The Journal of hand surgery*, **37**, 446–53.
- [35] Blythe, M., Stoffel, K., Jarrett, P., and Kuster, M. (2006) Volar versus dorsal locking plates with and without radial styloid locking plates for the fixation of dorsally comminuted distal radius fractures: A biomechanical study in cadavers. *The Journal of hand surgery*, **31**, 1587–93.
- [36] Willis, A., Kutsumi, K., Zobitz, M. E., and Cooney, W. P. (2006) Internal fixation of dorsally displaced fractures of the distal part of the radius. A biomechanical analysis of volar plate fracture stability. *The Journal of bone and joint surgery. American volume*, **88**, 2411–7.

- [37] Mehling, I., Müller, L., and Rommens, P. (2012) Biomechanische Vergleichsstudien von Implantatsystemen zur Versorgung distaler Radiusfrakturen: Welche Schlussfolgerungen ergeben sich für die klinische Praxis? *Handchir Mikrochir Plast Chir.*, **44**, 300–305.
- [38] Bathe, K. J. (1996) *Finite Element Procedures*. Prentice-Hall International Series, Prentice Hall.
- [39] Kluess, D. (2010) Finite Element Analysis in Orthopaedic Biomechanics. Moratal, D. (ed.), *Finite Element Analysis*, pp. 151–172, INTECH Open Access Publisher.
- [40] Oden, J. (2010) Finite element method. *Scholarpedia*, **5**, 9836.
- [41] Morgan, E. F. and Bousein, M. L. (2005) Use of finite element analysis to assess bone strength. *BoneKEy-Osteovision*, **2**, 8–19.
- [42] Taddei, F., Martelli, S., Reggiani, B., Cristofolini, L., and Viceconti, M. (2006) Finite-element modeling of bones from CT data: sensitivity to geometry and material uncertainties. *IEEE transactions on bio-medical engineering*, **53**, 2194–200.
- [43] Engelke, K., et al. (2008) Clinical use of quantitative computed tomography and peripheral quantitative computed tomography in the management of osteoporosis in adults: the 2007 ISCD Official Positions. *Journal of clinical densitometry : the official journal of the International Society for Clinical Densitometry*, **11**, 123–62.
- [44] Krestan, C. and Gruber, M. (2013) Quantitative Computertomographie (QCT). *Journal für Mineralstoffwechsel*, **20**, 59–65.
- [45] Augat, P. and Schorlemmer, S. (2006) The role of cortical bone and its microstructure in bone strength. *Age and ageing*, **35 Suppl 2**, ii27–ii31.
- [46] Tjong, W., Kazakia, G. J., Burghardt, A. J., and Majumdar, S. (2012) The effect of voxel size on high-resolution peripheral computed tomography measurements of trabecular and cortical bone microstructure. *Medical physics*, **39**, 1893–903.
- [47] Lengsfeld, M., Schmitt, J., Alter, P., Kaminsky, J., and Leppek, R. (1998) Comparison of geometry-based and CT voxel-based finite element modelling and experimental validation. *Medical Engineering & Physics*, **20**, 515–522.
- [48] Varga, P., Baumbach, S., Pahr, D., and Zysset, P. K. (2009) Validation of an anatomy specific finite element model of Colles’ fracture. *Journal of biomechanics*, **42**, 1726–31.
- [49] Lin, Y.-h., Lin, C.-l., Kuo, H.-n., Sun, M.-t., and Chen, A. C.-y. (2011) Biomechanical Analysis of Volar and Dorsal Double Locking Plates for Fixation in Comminuted Extra-articular Distal Radius Fractures : A 3D Finite Element Study. **32**, 349–356.
- [50] Vlcek, M., Landor, I., Horak, Z., Musil, V., Sosna, A., and Jonas, D. (2014) Mathematical modelling for the comparison of plate and intramedullary osteosynthesis stability in intraarticular distal radius fractures. *Bratislavské lekárske listy*, **115**, 107–11.
- [51] Cheng, H.-Y. K., Lin, C.-L., Lin, Y.-H., and Chen, A. C.-Y. (2007) Biomechanical evaluation of the modified double-plating fixation for the distal radius fracture. *Clinical biomechanics (Bristol, Avon)*, **22**, 510–7.

- [52] Mair, S., Weninger, P., Hogel, F., Panzer, S., and Augat, P. (2011) Stability of volar fixed-angle plating for distal radius fractures : Failure modes in osteoporotic bone. *Unfallchirurg*, **116**, 338–44.
- [53] Baumbach, S. F., Schmidt, R., Varga, P., Heinz, T., Vécsei, V., and Zysset, P. K. (2011) Where is the distal fracture line location of dorsally displaced distal radius fractures? *Journal of orthopaedic research : official publication of the Orthopaedic Research Society*, **29**, 489–94.
- [54] Baumbach, S. F., Dall’Ara, E., Weninger, P., Antoni, A., Traxler, H., Dörr, M., and Zysset, P. K. (2012) Assessment of a novel biomechanical fracture model for distal radius fractures. *BMC musculoskeletal disorders*, **13**, 252.
- [55] Crawley, M. J. (2007) *The R Book*. Wiley Publishing, 1st edn.
- [56] Pahr, D. H. and Zysset, P. K. (2009) From high-resolution CT data to finite element models: development of an integrated modular framework. *Computer Methods in Biomechanics and Biomedical Engineering*, **12**, 45–57.
- [57] Alliez, P., Rineau, L., Tayeb, S., Tournois, J., and Yvinec, M. (2014) 3D Mesh Generation. *CGAL User and Reference Manual*, CGAL Editorial Board, 4.5 edn.
- [58] Luisier, B., Dall’Ara, E., and Pahr, D. H. (2014) Orthotropic HR-pQCT-based FE models improve strength predictions for stance but not for side-way fall loading compared to isotropic QCT-based FE models of human femurs. *Journal of the mechanical behavior of biomedical materials*, **32**, 287–99.
- [59] Mitra, N. J., Gelfand, N., Pottmann, H., and Guibas, L. (2004) Registration of point cloud data from a geometric optimization perspective. *Proceedings of the 2004 Eurographics/ACM SIGGRAPH symposium on Geometry processing - SGP ’04*, New York, New York, USA, Jul., p. 22, ACM Press.
- [60] Chetverikov, D., Stepanov, D., and Krsek, P. (2005) Robust Euclidean alignment of 3D point sets: the trimmed iterative closest point algorithm. *Image and Vision Computing*, **23**, 299–309.
- [61] Besl, P. and McKay, H. (1992) A method for registration of 3-D shapes. *IEEE Transactions on Pattern Analysis and Machine Intelligence*, **14**, 239–256.
- [62] Gelfand, N., Mitra, N. J., Guibas, L. J., and Pottmann, H. (2005) Robust global registration. *Symposium on geometry processing*, **2**, 197.
- [63] Foley, J. D., van Dam, A., Feiner, S. K., and Hughes, J. F. (1990) *Computer graphics: principles and practice* (2nd ed.).
- [64] Schwiedrzik, J. J. and Zysset, P. K. (2013) An anisotropic elastic-viscoplastic damage model for bone tissue. *Biomechanics and modeling in mechanobiology*, **12**, 201–13.
- [65] Gross, T., Pahr, D. H., and Zysset, P. K. (2013) Morphology-elasticity relationships using decreasing fabric information of human trabecular bone from three major anatomical locations. *Biomechanics and modeling in mechanobiology*, **12**, 793–800.
- [66] Cowin, C. (1989) *Bone Mechanics*. CRC Press.

- [67] Wolfram, U., Gross, T., Pahr, D. H., Schwiedrzik, J., Wilke, H.-J., and Zysset, P. K. (2012) Fabric-based Tsai-Wu yield criteria for vertebral trabecular bone in stress and strain space. *Journal of the mechanical behavior of biomedical materials*, **15**, 218–28.
- [68] ASM Aerospace Specification (2014), Titanium Grade 4. <http://asm.matweb.com/search/SpecificMaterial.asp?bassnum=MTU040>.
- [69] SpringSolver (2013), Material List. <http://www.springsolver.com/materials.php>.
- [70] FDW Handelsgesellschaft (2014), Technisches Datenblatt SG 141 / PUR 145. <http://www.fdw.at/upload/4876676-FDW-SG-141-PUR-145.pdf>.
- [71] Bland, J. M. and Altman, D. G. (2010) Statistical methods for assessing agreement between two methods of clinical measurement. *International Journal of Nursing Studies*, **47**, 931–936.
- [72] McCall, T. A., Conrad, B., Badman, B., and Wright, T. (2007) Volar versus dorsal fixed-angle fixation of dorsally unstable extra-articular distal radius fractures: a biomechanic study. *The Journal of hand surgery*, **32**, 806–12.
- [73] Osada, D., Fujita, S., Tamai, K., Iwamoto, A., Tomizawa, K., and Saotome, K. (2004) Biomechanics in uniaxial compression of three distal radius volar plates. *The Journal of hand surgery*, **29**, 446–51.
- [74] Moazen, M., Mak, J. H., Jones, A. C., Jin, Z., Wilcox, R. K., and Tsiridis, E. (2013) Evaluation of a new approach for modelling the screw-bone interface in a locking plate fixation: a corroboration study. *Proceedings of the Institution of Mechanical Engineers. Part H, Journal of engineering in medicine*, **227**, 746–56.